JOURNAL OF GEOPHYSICAL RESEARCH: SOLID EARTH, VOL. 118, 4325–4344, doi:10.1002/jgrb.50321, 2013

Crustal and uppermost mantle structure in the central U.S. encompassing the Midcontinent Rift

Weisen Shen,[1] Michael H. Ritzwoller,[1] and Vera Schulte-Pelkum[2]

Received 23 April 2013; revised 1 August 2013; accepted 4 August 2013; published 28 August 2013.

[1] Rayleigh wave phase velocities across the western arm of the Midcontinent Rift (MCR) and surrounding regions are mapped by ambient noise (8–40 s) and earthquake tomography (25–80 s) applied to data from more than 120 Earthscope/USArray stations across the central U.S. Receiver functions also are computed for those stations using harmonic stripping. Joint Bayesian Monte Carlo inversion is applied to generate 3-D posterior distributions of shear wave speeds (Vsv) in the crust and uppermost mantle to a depth of about 150 km, providing an overview of the seismic structure of the MCR and adjacent structures. Three major structural attributes are identified: (1) There is a high correlation between the long-wavelength gravity field and shallow Vs structure, but the MCR gravity high is obscured by clastic sediments in the shallow crust. This is consistent with an upper crustal origin to the MCR gravity anomaly as well as other anomalies in the region. (2) Thick crust (>47 km) underlies the MCR, but there is a gradient Moho in the northern part of the rift and a sharp Moho in the south. Thickened crust beneath the MCR is evidence for postrifting compression with pure-shear deformation along the entire rift; along-rift differences in lower crustal structure may signify magmatic underplating in the northern rift. (3) Crustal shear wave speeds vary across the Precambrian sutures (e.g., Great Lakes Tectonic Zone, Spirit Lakes Tectonic Zone). This reveals the importance of Precambrian sutures in the subsequent tectonic evolution of the central U.S.

Citation: Shen, W., M. H. Ritzwoller, and V. Schulte-Pelkum (2013), Crustal and uppermost mantle structure in the central U.S. encompassing the Midcontinent Rift, *J. Geophys. Res. Solid Earth*, *118*, 4325–4344, doi:10.1002/jgrb.50321.

1. Introduction

[2] The most prominent gravity anomaly in the central U.S. [*Woollard and Joesting*, 1964] is a 2000 km long gravity high with two arms merging at Lake Superior and extending southwest to Kansas and southeast into Michigan. This anomaly has been determined to mark a late Proterozoic tectonic zone [*Whitmeyer and Karlstrom*, 2007]. Because of the existence of mantle-source magmatism and normal faults found along the anomaly, it has been generally accepted that this anomaly resulted from a continent rifting episode and as a consequence is known as the Midcontinent Rift system (MCR) [*Schmus*, 1992] or Keweenawan Rift system. Geochronological evidence shows that the rift initiated at about 1.1 Ga and cut through several crustal provinces [*Hinze et al*., 1997]. Although various geological and seismic studies have focused on the rift [*Hinze et al*., 1992; *Mariano and Hinze*, 1994; *Woelk and Hinze*, 1991; *Cannon et al*., 1989; *Vervoort et al*., 2007; *Hollings et al*., 2010; *Hammer et al*., 2010; *Zartman et al*., 2013], the mechanisms behind the opening and rapid deactivation and subsequent closure of the rift are still under debate. Fundamental questions, therefore, remain as to the nature and origin of the rift system [*Stein et al*., 2011].

[3] Figure 1 outlines the location of the western arm of the MCR and its neighboring geological provinces. The MCR can be thought of as being composed of three large-scale components: the western arm through Minnesota, Iowa, and Kansas; the Lake Superior arm; and the eastern arm through Michigan. Our focus here is on the western arm. A free-air gravity high defines its location (see 40 mGal anomaly contour in Figure 1b), but it divides further into three segments: a northern one extending from near the south shore of Lake Superior along the Wisconsin-Minnesota boundary, a southern one extending from northeastern to southeastern Iowa, and a small segment in Nebraska and Kansas. Marginal gravity minima flank the MCR and have been interpreted as a signature of flanking sedimentary basins [*Hinze et al*., 1992]. Gravity decreases broadly from 0–30 mGal in the north to −30 mGal in the south. Whether and how these gravity features relate to the structure of the crust and uppermost mantle is poorly understood.

[4] The western arm of the MCR remains somewhat more poorly characterized than the Lake Superior component of the MCR due to a veneer of Phanerozoic sediments [*Hinze et al*., 1997]. About two decades ago active seismic studies

[1]Department of Physics, University of Colorado Boulder, Boulder, Colorado, USA.
[2]Cooperative Institute for Research in Environmental Sciences and Department of Geological Sciences, University of Colorado Boulder, Boulder, Colorado, USA.

Corresponding author: W. Shen, Department of Physics, University of Colorado at Boulder, Boulder, CO 80309-0390, USA. (weisen.shen@colorado.edu)

2169-9313/13/10.1002/jgrb.50321

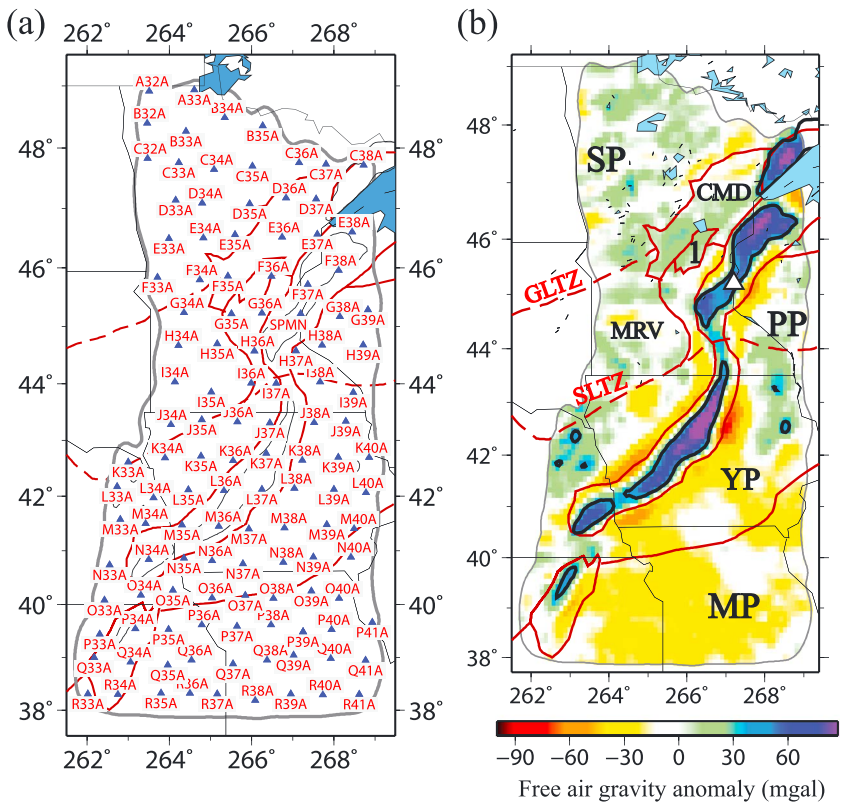

Figure 1. (a) The 122 seismic stations used in this study are named and shown with triangles. (b) The free-air gravity anomaly [*Pavlis et al*., 2012] is plotted in the background, with the 40 mGal level contoured with black lines to highlight the location of the major positive gravity anomaly along the Midcontinent Rift (MCR). Simplified tectonic boundaries are shown as solid dark red curves, which are identified with abbreviations: Superior Province (SP), Craton Margin Domain (CMD), Minnesota River Valley (MRV), Penokean Province (PP), Spirit Lake Tectonic Zone (SLTZ), Yavapai Province (YP), and Mazatzal Province (MP). A dashed line crossing the South Dakota and Minnesota border is the Great Lakes Tectonic Zone (GLTZ), which separates the Superior Province into the Superior Greenstone Terrane to the north and MRV to the south. The number "1" indicates the location of the east central Minnesota batholith.

were performed from northwestern Wisconsin to northeastern Kansas [*Chandler et al*., 1989; *Woelk and Hinze*, 1991] that revealed a structure similar to the Lake Superior component [*Hinze et al*., 1992]. These similarities include crustal thickening to more than 48 km and high-angle thrust faults that appear to be reactivated from earlier normal faults. *Van Schmus et al*. [1993] and *Cannon* [1994] attributed these features to a postrifting compressional episode during the Grenville orogeny.

[5] The MCR cuts across a broad section of geological provinces of much greater age. The Superior segment of the MCR is embedded in the Archean Superior Province (SP, 2.6–3.6 Ga), which continues into Canada. In Minnesota this province is subdivided by the Great Lakes Tectonic Zone (GLTZ) west of the MCR into the 2.6–2.75 Ga Greenstone-Granite Terrane in the north and the 3.4–3.6 Ga Gneiss Terrane or "Minnesota River Valley Subprovince" (MRV) in the south [*Sims and Petermar*, 1986]. During the Paleoproterozoic (1.8–1.9 Ga), the Penokean Province (PP) is believed to have been accreted to the southern edge of the Superior Province, adding vast foreland basin rocks and continental rocks along its margin. This is marked as a "craton margin domain (CMD)" [*Holm et al*., 2007] in Figure 1. From 1.7 to 1.8 Ga the Yavapai province was added to the southern Minnesota River Valley and the Penokean provinces, which drove overprinting metamorphism and magmatism along the continental margin to the north. The east central Minnesota batholith ("1" in Figure 1) is believed to have been created during this time [*Holm et al*., 2007], and this accretion produced the continental suture known as the Spirit Lake Tectonic Zone (SLTZ). Later (1.65–1.69 Ga), the Mazatzal Province (MP) was accreted to the Yavapai Province, producing another metamorphic episode south of the Spirit Lake Tectonic Zone. Overall, the 1.1 Ga rift initiated and terminated in a context provided by geological provinces ranging in age from 1.6 to 3.6 Ga. During the Phanerozoic, this region suffered little tectonic alteration.

[6] In this paper we aim to produce an improved, uniformly processed 3-D image of the crust and uppermost mantle underlying the western arm of the MCR and surrounding Precambrian geological provinces and sutures. The purpose is to provide information on the state of the lithosphere beneath the region using a unified, well-understood set of observational methods. We are motivated by a long list of unanswered questions concerning the structure of the MCR, including the following. (1) How are observed gravity anomalies related to the crustal and uppermost mantle structure

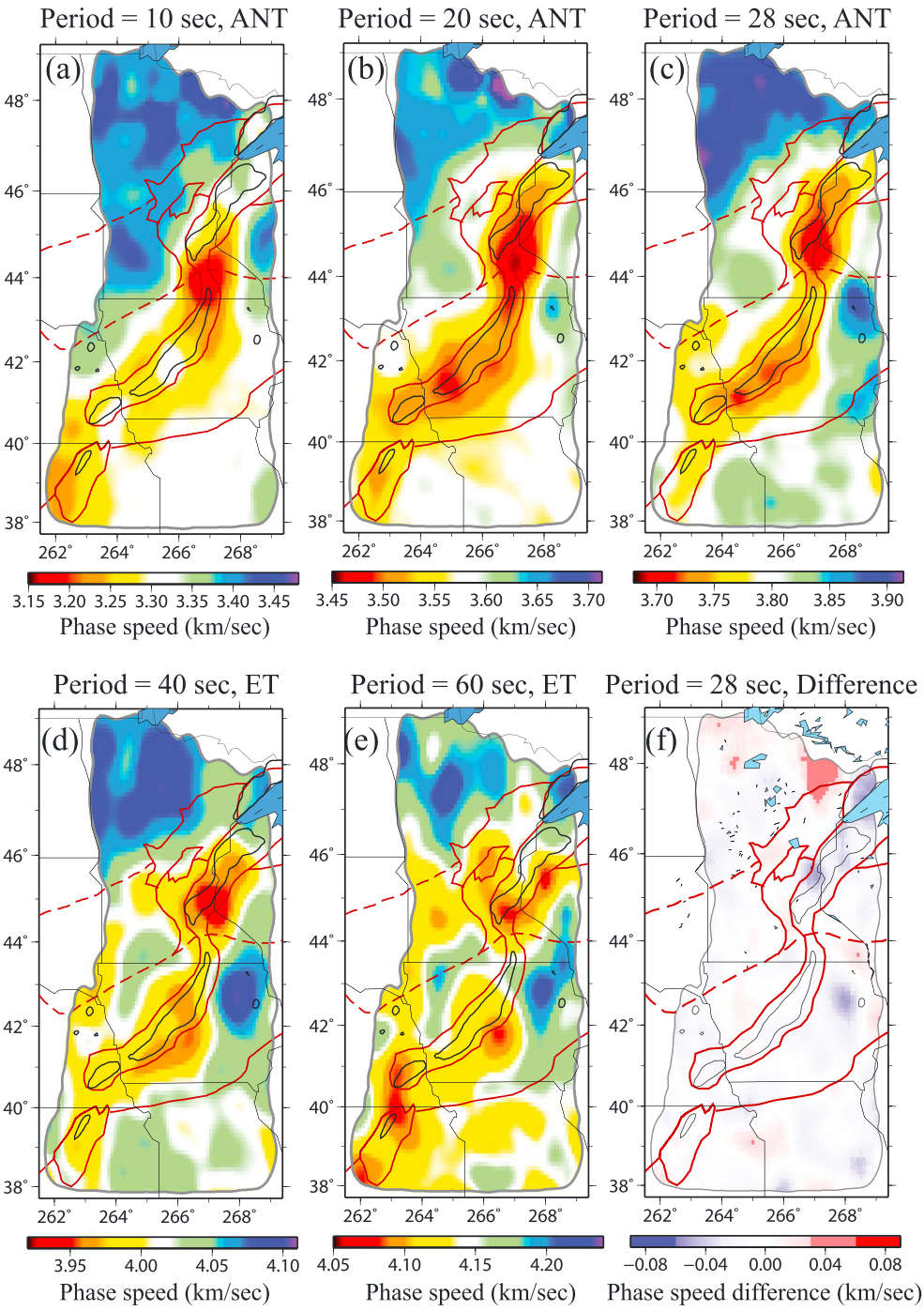

Figure 2. Rayleigh wave phase velocity maps from ambient noise tomography (ANT) and earthquake tomography (ET). Maps from ambient noise eikonal tomography at periods of (a) 10, (b) 20, and (c) 28 s. Maps at (d) 40 and (e) 60 s from teleseismic earthquake Helmholtz tomography. (f) Difference between the phase velocity map from ANT and ET at 28 s period.

of the region, particularly the gravity high associated with the MCR? (2) Is the crust thickened (or thinned) beneath the MCR, and how does it vary along the strike of the feature? (3) Is the MCR structurally a crustal feature alone, or do remnants of its creation and evolution extend into the upper mantle? (4) Are the structures of the crust and uppermost mantle continuous across sutures between geological provinces, or are they distinct and correlated with such provinces?

[7] These are challenging questions for passive source seismology (ambient noise and earthquake tomography). The MCR is long and narrow and a difficult target tomographically. Thermal anomalies associated with the rifting and subsequent closure of the MCR have thermally equilibrated, making the region relatively homogeneous compared, for example, with the western U.S. [e.g., *Shen et al.*, 2013a]. However, since 2010, the Earthscope/USArray Transportable Array (TA) left the tectonic western U.S. and rolled over the

region encompassing the western arm of the MCR, making it possible to obtain new information about the subsurface structure of this feature. The earlier deployment of USArray stimulated the development of new seismic data analysis and imaging methods. This includes ambient noise tomography [e.g., *Shapiro et al*., 2005; *Lin et al*., 2008; *Ritzwoller et al*., 2011] performed with new imaging methods such as eikonal tomography [*Lin et al*., 2009] as well as new methods of earthquake tomography such as Helmholtz tomography [*Lin and Ritzwoller*, 2011] and related methods [e.g., *Pollitz*, 2008; *Yang et al*., 2008b; *Pollitz and Snoke*, 2010]. New methods of inference have also been developed based on Bayesian Monte Carlo joint inversion of surface wave dispersion and receiver function data [*Shen et al*., 2013a] that yield refined constraints on crustal structure with realistic estimates of uncertainties. The application of these methods together have produced a higher-resolution 3-D shear velocity (Vs) model of the western U.S. [*Shen et al*., 2013b] with attendant uncertainties and have also been applied on other continents [e.g., *Zhou et al*., 2012; *Zheng et al*., 2011; *Yang et al*., 2012; *Xie et al*., 2013]. In this paper we utilize more than 120 TA stations that cover the MCR region to produce high-resolution Rayleigh wave phase velocity maps from 8 to 80 s period by using ambient noise eikonal and teleseismic earthquake Helmholtz tomography. We then jointly invert these phase velocity dispersion curves locally with receiver functions to produce a 3-D Vsv model for the crust and uppermost mantle beneath the western MCR and the surrounding region.

2. Data Processing

[8] The 122 USArray stations used in this study are shown in Figure 1a as black triangles, which evenly cover the study area with an average interstation distance of about 70 km. Based on this station set, we construct surface wave dispersion curves from ambient noise and earthquake data as well as receiver functions. Rayleigh wave phase velocity curves from 8 to 80 s period are taken from surface wave dispersion maps generated by eikonal tomography based on ambient noise and Helmholtz tomography based on teleseismic earthquakes. We also construct a back-azimuth independent receiver function at each station by the harmonic stripping technique. Details of these methods have been documented in several papers (eikonal tomography: *Lin et al*. [2009]; Helmholtz tomography: *Lin and Ritzwoller* [2011]; harmonic stripping: *Shen et al*. [2013a]) and are only briefly summarized here.

2.1. Rayleigh Wave Dispersion Curves

[9] We measured Rayleigh wave phase velocities from 8 to 40 s period from ambient noise cross correlations based on the USArray TA stations available from 2010 to May 2012. We combined the 122 stations in the study area with the TA stations to the west of the area [*Shen et al*., 2013b] in order to increase the path density. The ambient noise data processing procedures are those described by *Bensen et al*. [2007] and *Lin et al*. [2008] and produce more than 10,000 Rayleigh wave phase velocity curves in the region of study. As shown by *Yang and Ritzwoller* [2008] and many others, the azimuthal content of ambient noise in the U.S. is sufficient to estimate phase and group velocities for Rayleigh and Love waves reliably. At these periods (8 to 40 s) eikonal tomography [*Lin et al*., 2009] produces Rayleigh wave phase velocity maps with uncertainties based on ambient noise (e.g., Figures 2a–2c). For longer periods (25 to 80 s) Rayleigh wave phase velocity measurements are obtained from earthquakes using the Helmholtz tomography method [*Lin and Ritzwoller*, 2011] in which finite frequency effects are modeled. A total of 875 earthquakes between 2010 and 2012 with $M_s > 5.0$ are used, and on average each station records acceptable measurements (based on a SNR criterion) from about 200 earthquakes for surface wave analysis. Example maps are presented in Figures 2d and 2e. In the period band of overlap between the ambient noise and earthquake measurements (25 to 40 s) there is strong agreement between the resulting Rayleigh wave maps (Figure 2f). The average difference is ~ 1 m/s, and the standard deviation of the difference is ~ 12 m/s, which is within the uncertainties estimated for this period (~15 m/s).

[10] At 10 s period, at which Rayleigh waves are primarily sensitive to sedimentary layer thickness and the uppermost crystalline crust, a slow anomaly is seen in the gap between the northern and southern MCR and runs along the flanks of the MCR, particularly in the south. Wave speeds are high north of the Great Lakes Tectonic Zone (GLTZ) and average in the Mazatzal Province. Between 20 and 40 s, the most prominent feature is the low speed anomaly that runs along the MCR, as was also seen by F.F. Pollitz and W.D. Mooney (Mantle origin for stress concentration in the New Madrid Seismic Zone, submitted to *Earth and Planetary Science Letters*, 2013). This indicates low shear wave speeds in the lower crust/uppermost mantle and/or a thickened crust beneath the MCR. Higher wave speeds at these periods appear mostly north of the Great Lakes Tectonic Zone. At longer periods, the anomaly underlying the MCR breaks into northern and southern segments with the lowest wave speeds shift off the rift axis near the southern MCR. Most of our study region is outside the area covered by the short period dispersion maps from the earlier data by *Liang and Langston* [2008], so comparison with that study is impossible. With these Rayleigh wave phase speed dispersion maps at periods between 8 and 80 s, we produce a local dispersion curve at each station location. For example, the local Rayleigh wave phase velocity curve with uncertainties at station E33A in the southern Superior Province is shown in Figure 3a with black error bars. Other example Rayleigh wave curves are presented in Figures 3b–3f.

2.2. Receiver Function Processing

[11] The method we use to process receiver functions for each station is described in detail in *Shen et al*. [2013b]. For each station, we pick earthquakes from the years 2010, 2011, and 2012 in the distance range from 30° to 90° with $m_b > 5.0$. We apply a time domain deconvolution method [*Ligorria and Ammon*, 1999] to each seismogram windowed between 20 s before and 30 s after the *P* wave arrival to calculate radial component receiver functions with a low-pass Gaussian filter with a width of 2.5 s (pulse width ~ 1 s), and high-quality receiver functions are selected via an automated procedure. Corrections are made to both the time and amplitude of each receiver function, normalizing to a reference slowness of 0.06 s/km [*Jones and Phinney*, 1998]. Finally, only the first

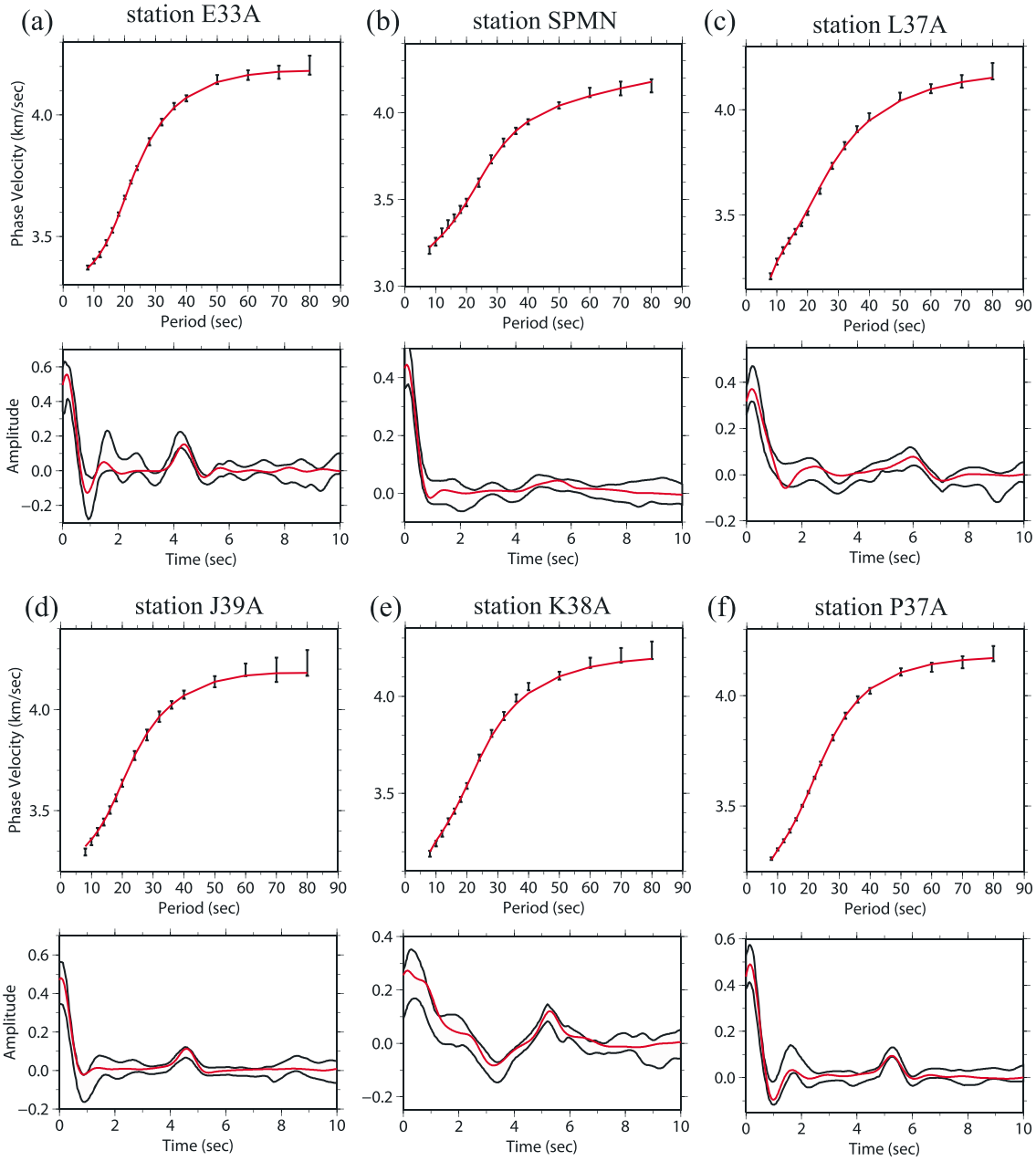

Figure 3. Examples of local Rayleigh wave phase velocity curves with uncertainty estimates (black error bars) and the azimuthally independent receiver functions (parallel black waveforms) are compared with predicted dispersion curves and receiver functions from the best fitting model at each location (red curves): (a) station E33A in the Southern Superior Province, (b) SPMN in the northern MCR, (c) L37A in the southern MCR, (d) J39A in northeastern Iowa east of the MCR, (e) K38A on the eastern flank of the southern MCR, and (f) P37A in the Mazatzal Province.

10 s after the direct *P* arrival is retained for further analysis. We compute the azimuthally independent receiver function, $R_0(t)$, for each station by fitting a truncated Fourier Series at each time over azimuth and removing (or stripping) the azimuthally variable terms using a method referred to as "harmonic stripping" by *Shen et al*. [2013b]. This method exploits the azimuthal harmonic behavior of receiver functions caused by sloping interfaces and anisotropy [e.g., *Girardin and Farra*, 1998; *Bianchi et al*., 2010]. After removing the azimuthally variable terms at each time, the RMS residual over azimuth is taken as the 1σ uncertainty at that time.

[12] On average, about 72 earthquakes satisfy the quality control provisions for each station across the region of study, which is about half of the average number of similarly high-quality recordings at the stations in the western U.S. [*Shen et al*., 2013b]. This reduction in the number of accepted receiver functions results primarily from the distance range for teleseismic *P* (30° to 90°), which eliminates many events from the southwest Pacific (e.g., Tonga). The number of retained earthquakes varies across the region of study, being highest toward the southern and western parts of the study region and lowest toward the north and east. At some stations

there are as few as 21 earthquake records retained, and receiver functions at 15 stations display a large gap in back-azimuth, which prohibits applying the harmonic stripping method. For these stations, we use a simple, directly stacked receiver function to represent the local average. Overall, the quality of the resulting azimuthally independent receiver functions is significantly lower than observed across the western U.S. by *Shen et al*. [2013a,2013b], where more than 100 earthquakes are typically retained for receiver function analysis, but is high enough to provide reliable information at nearly every station in the study region.

[13] Examples of receiver functions at six stations in the MCR region are shown in Figure 3 as parallel black lines that delineate the one standard deviation uncertainty at each time. At station E33A (Figure 3a) in the southern Superior Province, a clear Moho conversion appears at ~4.3 s after the direct *P* arrival, which indicates a distinct, shallow (~35 km) Moho discontinuity. In contrast, at station SPMN in the northern MCR (Figure 3b) only a subtle Moho Ps conversion is apparent, which suggests a gradient Moho beneath the station. In the southern MCR, the receiver function at station L37A (Figure 3c) has a Moho Ps signal at ~6 s, implying the Moho discontinuity is at over 45 km depth. At station J39A to the east of the MCR (Figure 3d), a Moho Ps conversion at ~4.5 s is observed, indicating a much thinner crust. At K38A, which is located in the gravity low of the eastern flank of the southern MCR (Figure 3e), a sediment reverberation appears after the *P* arrival. In the Mazatzal Province at station P37A (Figure 3f) a relatively simple receiver function is observed with a Moho Ps conversion at ~5.3 s, indicative of crust of intermediate thickness in this region.

3. Construction of the 3-D Model From Bayesian Monte Carlo Joint Inversion

[14] Here we briefly summarize the joint Bayesian Monte Carlo inversion of surface wave dispersion curves and receiver functions generated in the steps described in section 2. A 1-D joint inversion of the station receiver function and dispersion curve is performed on the unevenly distributed station grid, and then the resulting models from all stations are interpolated into the 3-D model using a simple kriging method, as described by *Shen et al*. [2013b].

3.1. Model Space and Prior Information

[15] We currently only measure Rayleigh wave dispersion, which is primarily sensitive to Vsv, so we assume the model is isotropic: Vsv = Vsh = Vs. However, the possible existence of positive crustal radial anisotropy (Vsh > Vsv) would mean that our Vs estimate is low relative to a Voigt average. The Vs model beneath each station is divided into three principal layers. The top layer is the sedimentary layer defined by three unknowns: layer thickness and Vs at the top and bottom of the layer with Vs increasing linearly with depth. The second layer is the crystalline crust, parameterized with five unknowns: four cubic B-splines and crustal thickness. Finally, there is the uppermost mantle layer, which is given by five cubic B-splines, yielding a total of 13 free parameters at each location. The thickness of the uppermost mantle layer is set so that the total thickness of all three layers is 200 km. The model space is defined based on perturbations to a reference model consisting of the 3-D model of *Shapiro and Ritzwoller* [2002] for mantle Vsv, crustal thickness and crustal shear wave speeds from CRUST 2.0 [*Bassin et al*., 2000], and sedimentary thickness from *Mooney and Kaban* [2010]. Because the reference sediment model is inaccurate in the region of study, we empirically reset the reference sedimentary thickness at stations that display strong sedimentary reverberations in the receiver functions. Similarly, in some regions where there is a gradient Moho we iteratively reset Moho depth in the reference model to the value from similar regions of the model without a gradient Moho (e.g., northern MCR crustal thickness in the reference model has been iteratively reset to the estimated crustal thickness of the southern MCR). Following *Shen et al*. [2013b], the Vp/Vs ratio is set to be 2 for the sedimentary layer and 1.75 in the crystalline crust/upper mantle (consistent with a Poisson solid). Density is scaled from Vp by using results from *Christensen and Mooney* [1995] and *Brocher* [2005] in the crust and *Karato* [1993] in the mantle. The Q model from the preliminary reference Earth model [*Dziewonski and Anderson*, 1981] is used to apply the physical dispersion correction [*Kanamori and Anderson*, 1977], and our resulting model is reduced to 1 s period. Increasing Q in the upper mantle from 180 to 280 will reduce the resulting Vs by less than 0.5% at 80 km depth.

[16] In addition to the choices made in parameterizing the model, we impose three prior constraints in the Monte Carlo sampling of model space. (1) Vs increases with depth at the two model discontinuities (base of the sediments and Moho). (2) Vs increases monotonically with depth in the crystalline crust. (3) $Vs < 4.9$ km/s at all depths. These prior constraints are imposed for two reasons. First, our philosophy is to seek simple models that fit the data, and we allow complications in structure only where required by the data. Therefore, we see our inversions as testing the hypothesis that the Earth conforms to the simplifications represented by these constraints. If we are able to fit the data with very simple models, then we possess no evidence for complexity beyond our parameterization and constraints. That does not mean that such complexity is nonexistent, however. If we are unable to fit aspects of the data, then we relax the constraints or generalize the parameterization accordingly. The strongest of these constraints is the second together with the choice of the B-spline parameterization in the crust, namely, the requirement that crustal shear wave speeds increase monotonically and continuously with depth through the crystalline crust. Discussion of whether this constraint may be too rigid in parts of the study region is presented in section 4.7. The second reason to apply the constraints is that they reduce the extent of model space, which both reduces the computational burden and yields error estimates that more closely reflect our belief in the estimated model.

[17] As described by *Shen et al*. [2013b], the Bayesian Monte Carlo joint inversion method constructs a prior distribution of models at each location defined by allowed perturbations relative to the reference model as well as the model constraints described above. Examples of prior marginal distributions for crustal thickness at the six example stations are shown as white histograms in Figure 4. The nearly uniform distribution of the prior illustrates that we impose weak prior constraints on crustal thickness.

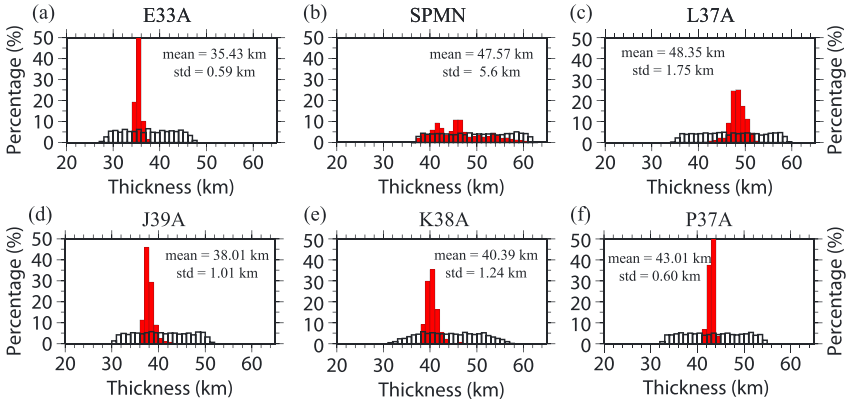

Figure 4. Prior and posterior distributions of crustal thickness for six example stations. (a) White histograms are the percentage distribution of the prior information for crustal thickness beneath station E33A. The red histogram centered at 35.43 km with $1\sigma = 0.59$ km represents the posterior distribution after the Bayesian Monte Carlo inversion. (b–f) Same as Figure 4a but for stations SPMN, L37A, J39A, K38A, and P37A, respectively.

3.2. Joint Monte Carlo Inversion and the Posterior Distribution

[18] Once the data are prepared and the prior model space is determined, we follow *Shen et al*. [2013b] and perform a Markov Chain Monte Carlo process to compute the posterior distribution. At each location, we consider at least 100,000 trial models in which the search is guided by the Metropolis algorithm. Models are accepted into the posterior distribution or rejected according to the square root of the reduced χ^2 value. A model m is accepted if $\chi(\mathrm{m}) > \chi_{\min} + 0.5$, where $\chi_{\min}$ is the χ value of the best fitting model. After the inversion, the misfit to the Rayleigh wave dispersion curve has a $\chi_{\min}$ value less than 1 for all the stations. Discussion of the fit to receiver function data is presented later in section 4.7 in the context of determining whether the piecewise smooth parameterization that we use is sufficient to model receiver functions.

[19] The principal output of the joint inversion at each station is the posterior distribution of models that satisfy the receiver function and surface wave dispersion data within tolerances that depend on the ability to fit the data and data uncertainties as discussed in the preceding paragraph. The statistical properties of the posterior distribution quantify model errors. In particular, the mean and standard deviation (interpreted as model uncertainty) of the accepted model ensemble are computed from the posterior distribution at each depth within the model. The posterior distribution represents both information from the data and prior constraints imposed on the inversion.

[20] Figure 4 presents posterior distributions for crustal thickness for six example stations as red histograms. Compared with the prior distributions (white histograms), the posterior distributions narrow significantly at five of the six stations, meaning that at these stations crustal thickness is fairly tightly constrained ($\sigma < 2$ km) with a clear Moho Ps conversion in the receiver function (Figure 3). The exception is station SPMN (Figure 3b) in the northern MCR where there is a weak Moho Ps conversion, but model uncertainty increases proportionally ($\sigma > 5$ km). In the six examples presented in Figure 4, crustal thickness ranges from about 35 to 48 km. Over the entire region of study, crustal thickness has a mean value of 44.8 km and an average 1σ uncertainty of about 3.3 km.

[21] Inversion results for the six example stations are shown in Figure 5. The clear Moho with small depth uncertainty at station E33A reflects the strong Moho Ps signal in the back-azimuth averaged receiver function (Figure 3a). Both the Rayleigh wave dispersion and the receiver function are fit well at this station (Figure 3a). In contrast, at station SPMN (Figure 5b) a gradient Moho appears in the model because the receiver function does not have a clear Moho Ps conversion (Figure 3b).

[22] The resulting models for the other four stations (L37A, J39A, K38A, P37A) are shown in Figures 5c–5f, and the fit to the data is shown in Figures 3c–3f. Station L37A is located near the center of the southern MCR. The receiver functions computed at this station show a relatively strong Moho Ps conversion at ~6 s after the direct *P* arrival, indicating a sharp Moho discontinuity at ~50 km depth with uncertainty of about 1.75 km. For station J39A in northeastern Iowa, the clear Ps conversion at ~5 s indicates a much shallower Moho discontinuity at ~40 km with an uncertainty of about 1 km. For station K38A near the eastern flank of the southern MCR, strong reverberations in the receiver function indicate the existence of thick sediments, but there is also a clear Moho Ps arrival. Finally, a clear Moho with uncertainty less than 1 km is seen beneath station P37A in the Mazatzal province.

[23] We perform the joint inversion for all 122 TA stations in the region of study and construct a mean 1-D model with uncertainties below each station. We then interpolate those 1-D models onto a regular $0.25° \times 0.25°$ grid by using a simple kriging method in order to construct a 3-D model for the study region [*Shen et al*., 2013a]. Simple kriging is only one possible method to interpolate the model between stations and may be optimal only in simplicity and computational efficiency. In simple kriging, model interpolation between stations is guided exclusively by the posterior distribution at all neighboring stations. Another possibility would be to use the surface wave phase speed maps to guide the

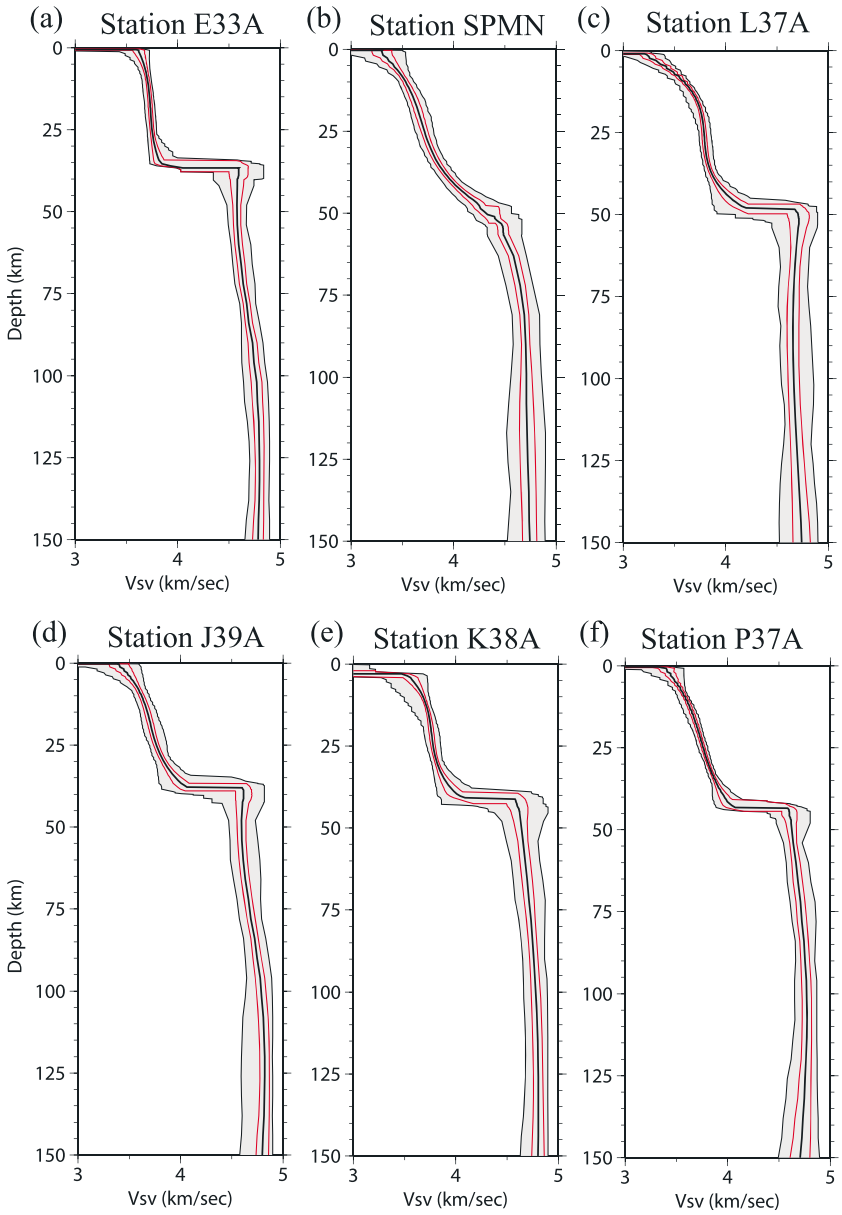

Figure 5. Resulting model ensembles that fit both Rayleigh wave and receiver function data for the six example stations of Figures 3 and 4. (a) The resulting model ensemble for station E33A. The average of the posterior distribution is shown as the black line near the middle of the grey corridor, which defines the full width of the posterior distribution at each depth. The red lines represent the 1σ width of the distribution. (b–f) Same as Figure 5a but for stations SPMN, L37A, J39A, K38A, and P37A, respectively.

interpolation because they exist on a grid finer than the station spacing. In this case, one would reperform the inversion at the interstation locations using only the phase speed information but with a prior distribution determined from the posterior distributions at the neighboring stations. We effected a simple version of this algorithm and found that differences relative to the kriging method are mostly subtle and largely confined to the shallow crust where the amplitude but not the distribution of features is increased somewhat. Therefore, this alternative method of interpolation does not present first-order changes in the model relative to the kriging method or affect the conclusions of this paper. We believe further development efforts of methods like this are advisable because of the general importance of assimilating data in inversions that may differ in type, grid location, and grid spacing, but such a method may be most useful in regions where interstation spacing is larger than the 70 km that characterizes the USArray TA.

[24] Maps of the 3-D model for various model characteristics are shown in Figures 6–8. Figure 6 presents map views of the 3-D model within the crust: average thickness and Vs of the sedimentary layer (Figures 6a and 6b, respectively), Vs at 10 km depth (Figure 6c), middle crust defined as the average in the middle one third of the crystalline crust (Figure 6d), and lower crust defined as the average from 80% to 100% of the depth to the Moho (Figure 6e). Moho depth, uncertainty in Moho depth, and the Vs contrast across the Moho (the average difference between Vs in the uppermost 1 km

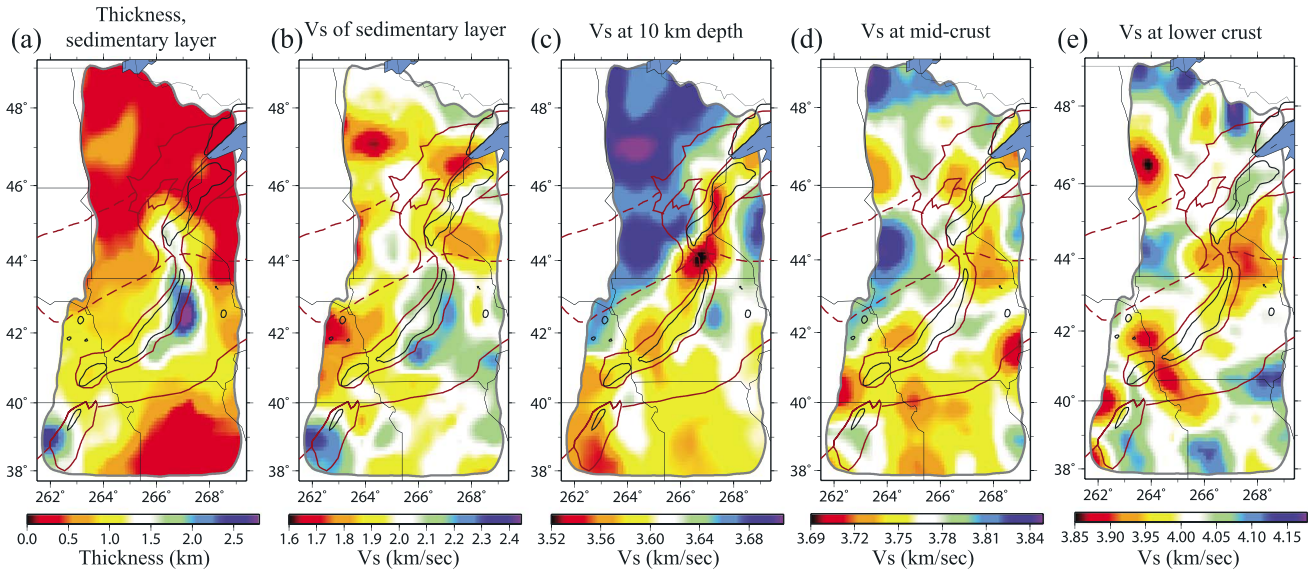

Figure 6. Maps of the mean of the posterior distribution for crustal structure of the study area. (a) Sedimentary thickness and (b) average shear wave speed. (c–e) Maps of Vsv at 10 km depth, in the middle crust (averaged in the middle one third of the crystalline crust), and in the lower crust (averaged for 80% to 100% of crustal depth), respectively.

of the mantle and lowermost 1 km of the crust) are shown in Figures 7a–7c. Deeper structures in the mantle are presented in Figure 8 with Vs maps at 80 km depth (Figure 8a) and 120 km (Figure 8b). Three vertical slices that cross the MCR are shown in Figure 9 along profiles identified as A-A′, B-B′, and C-C′ in Figure 8b. The model is discussed in more detail in section 4. Although the 3-D model extends to 200 km below the surface of the earth, the Vs uncertainties increase sharply with depth below 150 km due to the lack of vertical resolution. Therefore, we only discuss the top 150 km of the 3-D model.

4. Results and Discussion

4.1. Sedimentary Layer

[25] The sedimentary layer structure is shown in Figures 6a and 6b. Thick sediments (> 2 km) are observed near the eastern flank of the southern MCR, thinning southward. Another thick

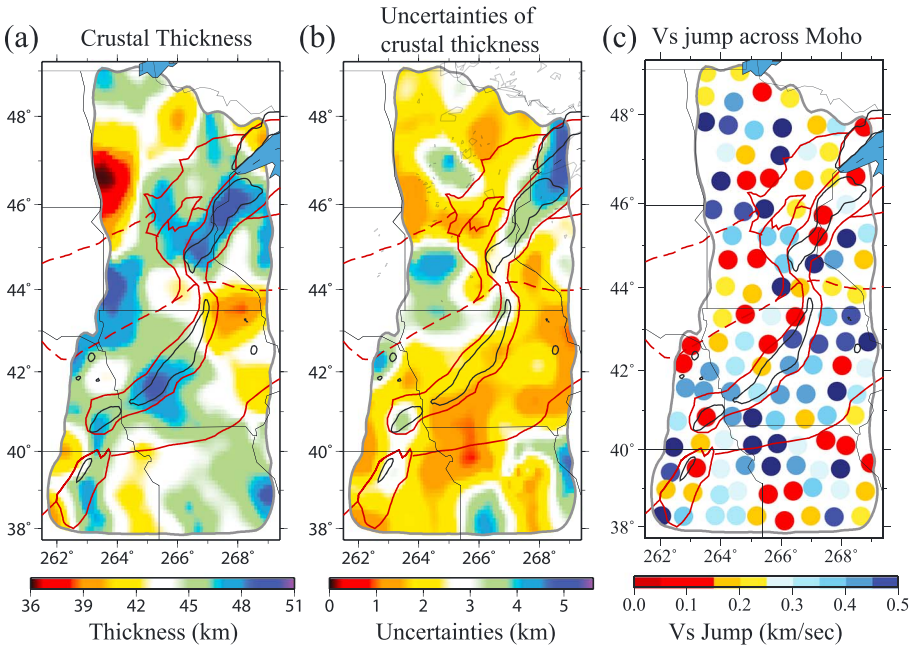

Figure 7. (a) Map of the mean of the posterior distribution for crustal thickness. (b) Map of the standard deviation of the posterior distribution for crustal thickness, interpreted as its uncertainty. (c) Mean of the posterior distribution for the shear velocity contrast across Moho (Vsv difference between the uppermost 1 km of the mantle and the lowermost 1 km of the crust) plotted at the station locations.

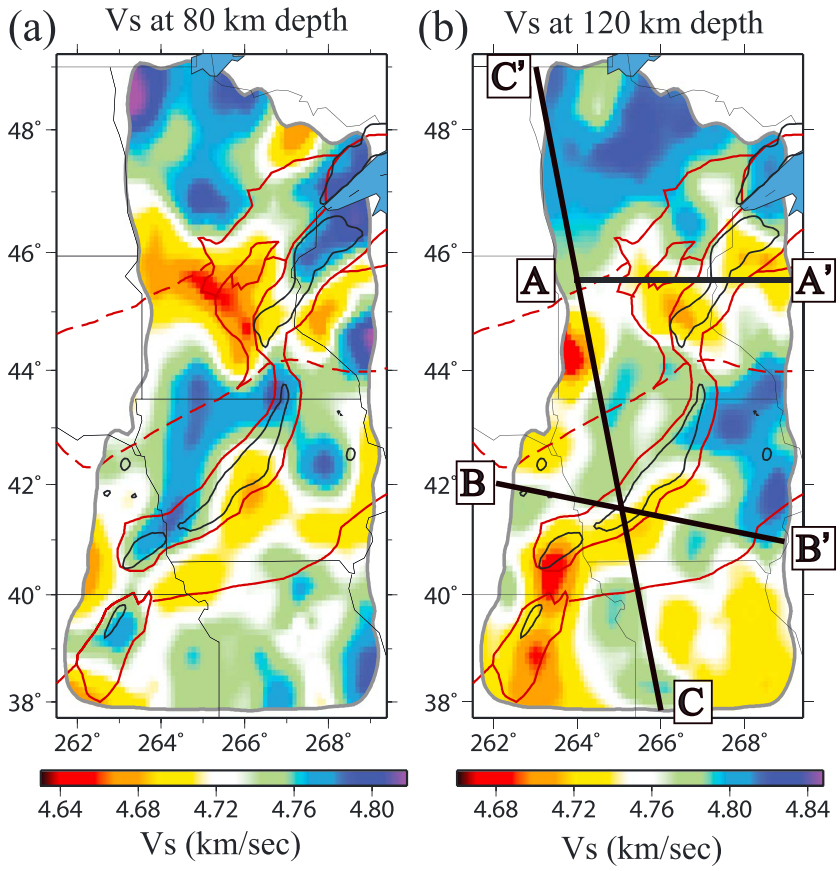

Figure 8. Maps of the mean of the posterior distribution for uppermost mantle Vsv at (a) 80 km depth and (b) 120 km depth. The black lines labeled A-A′, B-B′, and C-C′ indicate the locations of the three vertical transects presented in Figure 9.

sedimentary layer appears near the southern edge of the MCR in Kansas. In the rest of the area, the sediments are relatively thin (<1 km). Notably, sediments are thin in the region between the northern and southern MCR even though short-period Rayleigh wave phase speeds are slow (Figure 2a). This inference is guided by the receiver functions at nearby stations, which are inconsistent with strong sediments in this area. However, the resulting sedimentary distribution may be spatially aliased due to the high lateral resolution of the receiver functions (< 5 km) with a low spatial sampling rate from the station locations (~70 km). For this reason interpretation of data from the Superior Province Rifting Earthscope Experiment (SPREE) [*Stein*, 2011] is needed to more fully illuminate the shallow structure in this region.

[26] The receiver functions do indicate the existence of sediments with particularly low shear wave speeds in some areas. For example, strong reverberations observed in the receiver function for station E33A in the first 2 s may be fit by a Vs model with a thin (< 0.5 km) but slow Vs layer (< 1.8 km/s) near the surface (Figure 3a). Figure 6b shows the pattern of the inferred Vs in the sedimentary layer, which differs from the pattern of sedimentary thickness. Very slow sedimentary shear wave speeds are found in northern Minnesota, which may be due to the moraine associated with the Wadena glacial lobe [*Wright*, 1962]. Some of the slow sediments generate strong reverberations in the receiver functions that coincide in time with the Moho signal, resulting in large uncertainties in the crustal thickness map (Figure 7b). At some other stations, sedimentary reverberations do not obscure the Moho Ps arrival; e.g., K38A (Figure 3e). Sedimentary reverberations in the receiver functions can also be seen in Figure 9 beneath the Yavapai Province in transects B-B′ and C-C′, beneath the southern MCR in transect C-C′, and north of the southern MCR in transect C-C′.

4.2. Shallow Crystalline Crust and Correlation With the Observed Gravity Field

[27] The MCR gravity high (40 mGal anomaly outlined in the free-air gravity map of Figure 1) is poorly correlated with the shear velocity anomalies presented in Figures 6–8. Because positive density anomalies should correlate to positive velocity anomalies [e.g., *Woollard*, 1959; *Brocher*, 2005], the expectation is that high velocity anomalies underlie the MCR or the crust is thin along the rift. In fact, the opposite is the case. At 10 km depth, low velocity anomalies run beneath the rift and, on average, the crust is thickened under the rift. Our 3-D model, therefore, does not explain the gravity high that runs along the MCR. There are two possible explanations for this. First, the high-density bodies that cause the gravity high may be too small to be resolved with surface wave data determined from the station spacing presented by the USArray. Second, small high shear wave speed bodies that cause the gravity high may be obscured by sediments

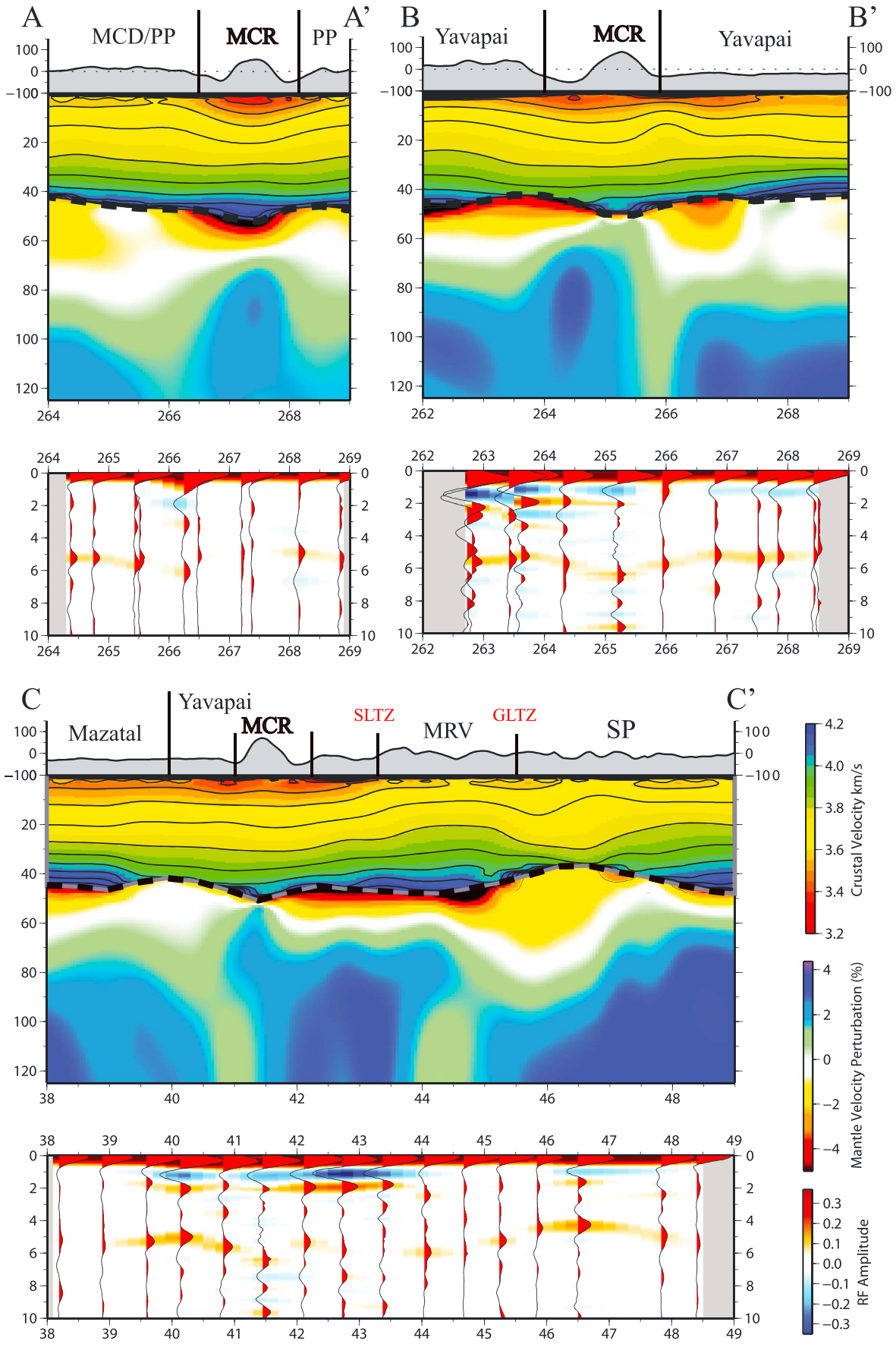
A
MCD/PP
MCR
PP
A'
B
Yavapai
MCR
Yavapai
B'
C
Mazatal
Yavapai
MCR
SLTZ
MRV
GLTZ
SP
C'
Crustal Velocity km/s
Mantle Velocity Perturbation (%)
RF Amplitude

Figure 9

in and adjacent to the rift. We believe the latter is the more likely cause of the anticorrelation between observed gravity anomalies and uppermost crustal shear velocity structure beneath the rift. If this is true, however, the high-density bodies that cause the gravity high probably would be in the shallow crust, or else they would imprint longer period maps that are less affected by sediments. This is consistent with the study of *Woelk and Hinze* [1991], who argue that the uppermost crust beneath the MCR contains both fast igneous rocks and slow clastic rocks. Under this interpretation, shallow igneous rocks must dominate the gravity field while the clastic rocks dominate the shear wave speeds. A shallow source for the gravity anomaly is also supported by the observation that the eastern arm of the MCR, which is buried under the Michigan Basin, has a much weaker gravity signature than the western arm imaged in this study [*Stein et al*., 2011].

[28] The 3-D shear velocity model is better correlated with the longer wavelengths in the gravity map (Figure 1), which displays a broad gradient across the region [*Frese et al*., 1982]. The free-air gravity southeast of the MCR is lower (−30 mGal) than in the northwestern part of the map (10–20 mGal). It has been argued that this gradient is not due to variations in Precambrian structure across the sutures [*Hinze et al*., 1992] but may be explained by a density difference in an upper crustal layer. Our results support an upper crustal origin because the correlation of high shear velocities with positive long-wavelength gravity anomalies exists primarily at shallow depths. At 10 km depth, which is in the uppermost crystalline crust (Figure 6c), the most prominent shear velocity feature is a velocity boundary that runs along the western flank of the MCR. This follows the Minnesota River Valley Province-Yavapai Province boundary in the west and the northeastern edge of the Craton Margin Domain in the east. North of this boundary, Vs is between 3.65 and 3.7 km/s in the southern Superior Province, while to the south it decreases to between 3.5 and 3.6 km/s in the Minnesota River Valley, Yavapai Province, and Mazatzal Province. This boundary lies near the contrast in free-air gravity. Similar features do not appear deeper in the model (Figures 6d, 6e, and 7).

[29] Because receiver functions are sensitive to the discontinuity between the sediments and the crystalline crustal basement, the commonly unresolved trade-off between crustal structure and deeper structure in traditional surface wave inversions [e.g., *Zheng et al*., 2011; *Zhou et al*., 2011] is ameliorated in the model we present here, and smearing of sedimentary velocities into the crystalline crust (e.g., Figure 6c) should not be strong. The observed high correlation of Vs with the long-wavelength gravity field supports this conclusion. Therefore, we believe that the very slow anomaly (< 3.5 km/s) that is observed in the gap between the northern and southern MCR at 10 km depth (Figure 6c) does in fact reside in the crystalline crust and is not a smearing effect of sediments to greater depth. It is not clear to us, however, why such low shear wave speeds appear in the upper crust at this location.

[30] Finally, there are also correlations between shallow Vs structure and short wavelength gravity anomalies. In the gravity map, the lowest amplitudes appear near station K38A on the eastern flank of the southern MCR where thick sediments are present in the model (Figure 5e). Thus, local gravity minima may be due to the presence of local sediments at this point.

4.3. Relationship Between Precambrian Sutures and Observed Crustal Structures

4.3.1. Great Lakes Tectonic Zone

[31] In the northern part of the study region, the Great Lakes Tectonic Zone (GLTZ) suture lies between the 2.7–2.75 Ga greenstone terrane to the north and the 3.6 Ga granulite-facies granitic and mafic gneisses Minnesota River Valley subprovince to the south, cutting the southern end of Superior Province into two subprovinces [*Morey and Sims*, 1976]. The eastern part of Great Lakes Tectonic Zone in our study region is covered by the Craton Margin Domain (CMD of Figure 1), which contains several structural discontinuities [*Holm et al*., 2007].

[32] Beneath this northernmost suture, a Vs contrast is observed in the 3-D model through the entire crust, with the contrast becoming stronger with depth. In the upper crust (Figure 6c), Vs is ~3.7 km/s beneath the Superior Province (SP) greenstone terrane and ~3.68 km/s beneath the Minnesota River Valley (MRV) with a relatively slow Vs belt beneath the eastern part of the suture. In the middle crust (Figure 6d), the Vs contrast is stronger. A fast anomaly (> 3.8 km/s) is observed beneath the MRV itself, perhaps indicating a more mafic middle crust, while in the north the SP is about 0.08 km/s slower than the MRV. This difference across the Great Lakes Tectonic Zone strengthens with depth to about 0.15 km/s in the lowermost crust (Figure 6e).

[33] These variations in crustal structure are also reflected in Moho depth, which is discussed further in section 4.4. North of the GLTZ, a clear, large-amplitude Moho signal is seen as early as 4.3 s (Figure 3a), although the receiver functions at some stations display large reverberations from the thin slow sediments. Combined with relatively fast phase velocities observed at 28 s period in this area, the inversion yields a relatively shallow Moho at about 36 km depth at station E33A and neighboring points. To the south of the GLTZ, thicker crust is found in the MRV with an average crustal thickness of about 46 km with a maximum thickness of about 48 km. The average uncertainties of crustal thickness in the MRV are greater than 3 km suggesting that the Moho is more of a gradient than a sharp boundary (Figure 7c). A seismic reflection study in this area [*Boyd and Smithson*, 1994] reveals localized Moho layering probably due to mafic intrusions related to post-Archean crustal thickening events in this area. Our large Moho depth and fast middle to lower crust (Figures 6d and 6e) are consistent with this interpretation.

Figure 9. Vertical transects of the means of the posterior distribution of Vsv along profiles A-A′, B-B′, and C-C′ whose locations are identified in Figure 8b. In the upper panel of each pair, absolute shear velocity (km/s) is shown in the crust, the Moho is identified by the thick dashed line, and percent perturbation relative to 4.65 km/s is presented in the mantle. In the lower panel of each pair, receiver functions at stations close to the transects are shown as black waveforms and filled with warm color for positive amplitudes and cool colors for negative amplitudes.

4.3.2. Spirit Lakes Tectonic Zone

[34] The boundary between the Superior (SP) and the Yavapai (YP) provinces is the Spirit Lakes Tectonic Zone (SLTZ), which extends east through the middle of the MCR into Wisconsin. East of the MCR, the SLTZ separates the Penokean Province to the north from the Yavapai Province to the south. As described in section 4.2, west of the MCR this suture forms a boundary within the upper crystalline crust that correlates with the transition from mild gravity highs to the north to gravity lows to the south. The Yavapai province is the region with thickest sediments across the region. Structural differences between the two provinces across the suture are particularly striking at 10 km depth but continue into the lower crust, with faster Vs in the Minnesota River Valley subprovince and slower Vs in the Yavapai. In terms of Moho topography, the Yavapai Province has relatively thinner crust (~44–45 km) than the Minnesota River Valley, particularly east of the southern MCR (~39 km). For example, the receiver function at station J39A (Figure 3d) displays a clear Moho Ps conversion at about 4.5 s after the direct *P* arrival. The resulting model for station J39A is shown in Figure 4d with a crustal thickness of about 38 ± 1.5km. This is the thinnest crust in the vicinity of the rift but is still deeper than in the Greenstone terrane in the western part of the Superior Province.

4.3.3. Boundary Between the Yavapai and Mazatzal Provinces

[35] The third and southernmost suture in the study region is the boundary between the Yavapai (YP) and Mazatzal provinces (MP) near the Iowa-Missouri border, extending in the NE-SW direction. Compared with the structural variations across the more northerly sutures, the variations across this suture are more subtle in both crustal velocities and crustal thickness. However, lower crustal Vs (Figure 6e) is slower (< 4 km/s) in the YP than it in the MP (> 4 km/s), and the velocity jump across Moho (Figure 7c) is larger in the YP, on average.

[36] In summary, the three major Precambrian sutures in the region are associated with crustal seismic structural variations, especially across the northern (GLTZ) and middle (SLTZ) sutures in the MCR region. Later cumulative metamorphism of early Proterozoic accretionary tectonics [*Holm et al*., 2007] may have obscured structural variations across the Yavapai-Mazatzal boundary at least in the shallow crust.

4.4. Variations in Crustal Thickness

[37] A clear and profound difference between average crustal and mantle shear wave speeds is observed across the entire region of study, as Figures 6d and 8a show. Average midcrustal shear wave speeds are about 3.76 km/s, whereas at 80 km depth they average about 4.72 km/s, nearly 1 km/s higher. However, we seek to determine crustal thickness where and if a jump in velocity occurs between the crust and uppermost mantle. The inference of this jump is guided principally by the receiver functions. An advantage of the joint inversion of surface wave dispersion and receiver functions is the amelioration of trade-offs that occur near structural discontinuities such as the base of the sediments and the Moho, which hamper inversion of surface wave data alone. As argued by *Shen et al*. [2013a, 2013b] and many others [e.g., *Bodin et al*., 2012; *Lebedev et al*., 2013], estimates of depth to Moho as well as the velocity contrast across it are greatly improved. But a clear Moho Ps converted phase is not observed at every station. Where it is observed, there is evidence for a jump of seismic velocities between the crust and uppermost mantle and we can estimate crustal thickness with considerable accuracy. Where this phase is not observed (e.g., Figure 3b), we have evidence that the transition between crustal and mantle shear wave speeds is probably gradual, which we refer to as a gradient Moho (e.g., Figure 5b). In these places, crustal thickness is not well defined, which may result from underplating or interleaving of crustal and mantle rocks in a finite Moho transition zone. In both instances whether we observe or do not observe a clear Moho Ps conversion on the receiver function, our estimate of the uncertainty in crustal thickness reflects our knowledge (e.g., Figure 7b).

[38] Therefore, our discussion of crustal thickness begins with an assessment of where we have definite information from receiver functions for a discrete jump in seismic wave speeds from the crust to the mantle and, hence, can estimate crustal thickness accurately. We present this information in Figure 7c as an estimate of the jump in shear wave speeds from the crust to the uppermost mantle. Stations at which this jump is below about 0.15 km/s (colored red in Figure 7c) are located where no Moho Ps conversion is seen and, hence, where there is a gradient Moho. Stations where the jump is larger than about 0.25 km/s (colored blue in Figure 7c) represent a clear sharp Moho. Stations underlain by a gradient Moho are scattered throughout the study region and number 22 of the 122 stations we used (or just less than 20% of the region). The locations of these stations are highly correlated with estimates of large uncertainty in crustal thickness (Figure 7b).

[39] We make two observations about the location of a gradient or a sharp Moho across the region. First, a sharp Moho is observed beneath the southern MCR but not beneath the northern MCR. Uncertainties in crustal thickness for the northern segment of the MCR are larger (> 4km) than for the southern segment (<2 km), as Figure 7b shows. Between the northern and southern segments, there is a shallow Moho (< 42 km) that extends eastward to the eastern Penokean Orogen and perhaps further east. Second, a sharp Moho is observed across much of the Yavapai province, whereas a gradient Moho is seen beneath much of the Minnesota River Valley province, which is consistent with a previous reflection seismic survey in the area [*Boyd and Smithson*, 1994].

[40] Figure 7a presents the resulting map of Moho topography and shows that the MCR is estimated to have a deep Moho (>47 km, peaking at ~50 km) in all three segments (Wisconsin/Minnesota, Iowa, Nebraska/Kansas), although crustal thickness in the northern MCR is not well determined because it is a gradient Moho. The crust beneath the MCR is about 5 km thicker, on average, than crustal thickness averaged across the study region. For the northern MCR, the crustal thickening mostly occurs within the gravity anomaly and extends to the northeastern edge of the Craton Margin Domain. In the southern MCR, crustal thickening is not uniform along the rift but is most pronounced in the southern half of this segment. For the Nebraska/Kansas segment, thickened crust (> 47 km) is also present, which is consistent with a previous reflection study for this area [*Woelk and Hinze*, 1991], although the northernmost part of this small region appears to have a gradient Moho. Analyzing older

data, *Moidaki et al*. [2013] also measured crustal thickness using Ps information and inferred locally thick crust (~53 km thick) beneath a narrow section of the southern MCR near 41.5N, 94.5W, which is near the area with the thickest crust we find beneath the southern MCR (Figure 7a).

[41] Notable crustal thickness variations are observed throughout the rest of the study area as well: a significantly thinned crust is seen near the western border of Minnesota within the Superior Province, which changes to a thick crust with a gradient Moho at about 50 km depth in the Gneiss Terrane of the Minnesota River Valley to the south. Another gradient Moho is observed north of the Great Lakes Tectonic Zone in the Superior Province. Further south, crustal thickness lies between 42 and 46 km in the Mazatzal Province.

[42] Three transects (identified as A-A′, B-B′, and C-C′ in Figure 8b) across the MCR are presented as pairs of panels in Figure 9. In the top half of each pair, absolute Vs in the crust beneath the three transects is shown with 0.1 km/s contours outlined by black lines and the Moho identified by a thick dashed line. In the mantle, Vs is shown as the percent perturbation relative to 4.65 km/s. Transects A-A′ and B-B′ cut the northern and southern segments of the MCR, respectively, and transect C-C′ cuts across the study region in the N-S direction and intersects with transect B in the southern MCR. In the lower half of each pair of panels of Figure 9, receiver function waveforms are shown for stations within a distance to each transect of 0.4°. We observe in the receiver functions two major features beneath the MCR. (1) As noted previously, Moho Ps conversion across the northern MCR (A-A′) is obscure. (2) There is a clearer Moho Ps conversion at ~6 s for the southern MCR (B-B′ and C-C′). As a result of the gradient Moho beneath the northern MCR, crustal thickness is poorly determined (1σ uncertainty > 4 km), lowermost crustal wave speeds are fast (> 4 km/s), and uppermost mantle wave speeds are slow (< 4.4 km/s). It is possible that this layer results from magmatic intrusion or underplating [*Furlong and Fountain*, 1986]. However, the underplating cannot be continuous along the entire MCR, because beneath the southern MCR this intermediate-velocity Vs layer is not present. In the adjacent area, another gradient Moho feature is seen beneath the Minnesota River Valley, with a Moho Ps conversion in the receiver functions that is weaker than those in the Superior or Yavapai Provinces (transect C-C′). This is consistent with a seismic reflection study in this subprovince [*Boyd and Smithson*, 1994] where Moho layering has been inferred due to mafic intrusion in the lower crust. The other features seen in these transects include the relatively thin crust (~40 km) near the flanks of the MCR (e.g., SMCR-Yavapai boundary) and in the southern Superior Province north of the Great Lakes Tectonic Zone. The latter region is the thinnest crust across the area of study (<38 km), and the cause of this thinning deserves further investigation.

4.5. Evidence That the MCR Is a Compressional Feature

[43] Currently active rifts such as the East African Rift [e.g., *Braile et al*., 1994; *Nyblade and Brazier*, 2002], the Rio Grande Rift [e.g., *West et al*., 2004; *Wilson et al*., 2005; *Shen et al*., 2013a], the West Antarctic Rift [*Ritzwoller et al*., 2001], and the Baikal rift [*Thybo and Nielsen*, 2009] as well as hot spots [e.g., Snake River Plain; e.g., *Shen et al*., 2013a] show crustal thinning. At some locations the thinned crust has been rethickened by mafic crustal underplating, for example, the Baikal rift [*Nielsen and Thybo*, 2009] and perhaps also the Lake Superior portion of the MCR [*Cannon et al*., 1989]. Although thermal anomalies dominantly produce low Vs in the mantle underlying active rifts [e.g., *Bastow et al*., 2005], compositional heterogeneity in the crust due to mafic underplating and intrusions can overcome the thermal anomaly to produce high crustal wave speeds even in currently active regions. After the thermal anomaly has equilibrated, as it has had time to do beneath the MCR, high crustal wave speeds would be expected. In actuality, we observe a thickened and somewhat slow crust within the MCR. We discuss here evidence that the observed crustal characteristics reflect the compressional episode that followed rifting [*Cannon*, 1994].

[44] The presence of low velocities in the upper and middle crust and crustal thickening beneath the MCR has been discussed above (e.g., Figures 6–8). Figure 9 presents vertical profiles along with receiver functions profiles shown for reference. Transect A-A′, extending from the Superior Province to the Penokean Province, illustrates that the upper crust beneath the rift is slightly slower than beneath surrounding areas and the crust thickens to about 50 km. In the upper and middle crust, lines of constant shear wave speed bow downward beneath the northern MCR, but this is not quite as clear in the southern MCR as transects B-B′ and C-C′ illustrate. The gradient Moho beneath transect A-A′ appears as lower Vs in the uppermost mantle in Transect A-A′. The sharper Moho beneath transects B-B′ and C-C′ appears as higher Vs in the uppermost mantle.

[45] These observations of a vertically thickened crust with the downward bowing of upper crustal velocity contours contradict expectations for a continent rift. They are, in fact, more consistent with vertical downward advection of material in the crust, perhaps caused by horizontal compression and pure-shear thickening. Geological observations and seismic reflection studies in the region also indicate a compressional episode occurring after rifting along the MCR. (1) Thrust faults form a horst-like uplift of the MCR, showing crustal shortening of about 20 to 35 km after rifting [*Anderson*, 1992; *Cannon and Hinze*, 1992; *Chandler et al*., 1989; *Woelk and Hinze*, 1991]. (2) Uplift evidence from anticlines and drag folds along reverse faults are also observed [*Fox*, 1988; *Mariano and Hinze*, 1994]. The horst-like uplift combined with reverse faults have been dated to circa 1060 Ma [*Bornhorst et al*., 1988; *White*, 1968; *Cannon and Hinze*, 1992], which is about 40 Ma after the final basalt intrusion [*Cannon*, 1994]. (3) Seismic reflection studies show a thickened crust beneath certain transects [Lake Superior: *Cannon et al*., 1989; Kansas: *Woelk and Hinze*, 1991].

[46] In summary, we argue from our 3-D model combined with these other lines of evidence that the present-day MCR is a compressional feature in the crust. The compressive event thickened the crust beneath the MCR and may have advected material downward in the crust. More speculatively, rifting (circa 1.1 Ga) followed by compression may have weakened the crust, which allowed for the extensive volcanism in the neighboring Craton Margin Domain that appears to have occurred in response to continental accretion to the south [*Holm et al*., 2007].

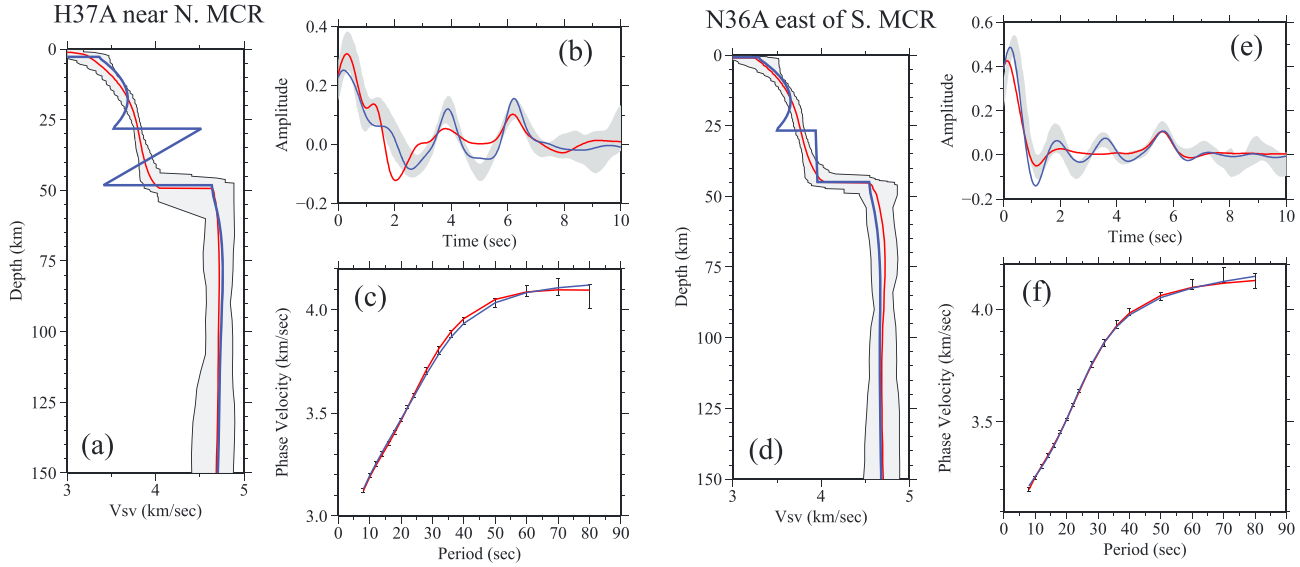

Figure 10. Comparison of models and data fit with and without a midcrustal discontinuity at two (H37A, N36A) of the four stations needing the discontinuity. (a, d) Like Figure 5 but where the model ensemble (grey shaded region) and best fitting model (red line) are compared with the best fitting model containing the midcrustal discontinuity. (b, e) Fit to the observed receiver function (grey shaded region) from the model with (blue line) and without (red line) the midcrustal discontinuity. (c, f) Fit to the observed Rayleigh wave phase velocity curve (one standard deviation error bars) from the model with (blue line) and without (red line) the midcrustal discontinuity.

[47] A potential alternative to tectonic compression as a means to produce crustal thickening beneath the MCR may be magmatic underplating that occurred during the extensional event that created the rift [e.g., *Henk et al.*, 1997]. Although the gradient Moho that is observed beneath parts of the northern MCR may be consistent with magmatic underplating, the clear Moho with the large jump in velocity across it in the southern MCR is at variance with underplating. The general absence of high velocity, presumably mafic, lower crust also does not favor magmatic intrusions into the lower crust. Thus, although magmatic underplating cannot be ruled out to exist beneath parts of the MCR, particularly in the north, it is an unlikely candidate for the unique cause of crustal thickening along the entire MCR. In addition, it cannot explain the downward bowing of shear velocity isolines in the upper and middle crust.

4.6. Uppermost Mantle Beneath the Region

[48] Not surprisingly for a region that has not undergone tectonic deformation for more than 1 Gyr, the upper mantle beneath the study region is seismically fast. The average shear wave speed at 100 km depth beneath the study region is 4.76 km/s. By comparison, at the same depth the upper mantle beneath the U.S. west of 100°W is 4.39 km/s. The slowest Vs is about 4.62 km/s at 80 km depth near the border of the east central Minnesota batholith. This is still faster than the Yangtze Craton (4.3 km/s at 140 km depth) [*Zhou et al.*, 2012] or the recently activated North China Craton (~4.3 km/s at 100 km, [*Zheng et al.*, 2011] but is similar to the Kaapvaal craton in South Africa [*Yang et al.*, 2008a]. The RMS variation across the region of study is about 0.05 km/s, which is much less than the variation across the western U.S. (RMS of 0.18 km/s). Thus, mantle variability across the central U.S. is small in comparison to more recently deformed regions.

[49] Although upper mantle structural variation is relatively small across the study region, Figures 8 and 9 show that prominent shear velocity anomalies are still apparent. In general, the Vs structure of the uppermost mantle is less related to the location of the Precambrian provinces and sutures than is crustal structure. One exception is deep in the model (120 km, Figure 8) where there is a prominent velocity jump across the Great Lakes Tectonic Zone. The principal mantle anomalies appear as two low velocity belts. One is roughly contained between the Great Lakes Tectonic Zone and the Spirit Lakes Tectonic Zone and then spreads into the Penokean Province east of the northern MCR. The other extends along the southern edge of the Southern and the Nebraska/Kansas segments of the MCR, particularly at depths greater than 100 km. Beneath the MCR itself, shear wave speeds in the uppermost mantle are variable. The main high velocity anomaly exists beneath the Superior Province with the shape varying slightly with depth. This anomaly terminates at the Great Lakes Tectonic Zone, being particularly sharp at 120 km depth. The jump in velocity at the Great Lakes Tectonic Zone is seen clearly in transect C-C′ (Figure 9c).

[50] There are three major factors that contribute to variations in isotropic shear wave speeds in the uppermost mantle: temperature, the existence of partial melt or fluids, and composition [e.g., *Saltzer and Humphreys*, 1997]. The fast average Vs in the upper mantle compared with tectonic regions and recently rejuvenated lithosphere suggests the lack of partial melt. Similarly, velocity anomalies in the region probably do not have a tectonothermal origin because they have had time to equilibrate in the past 1.1 Ga. However, low velocity anomalies at greater depth may still reflect thinner lithosphere, which

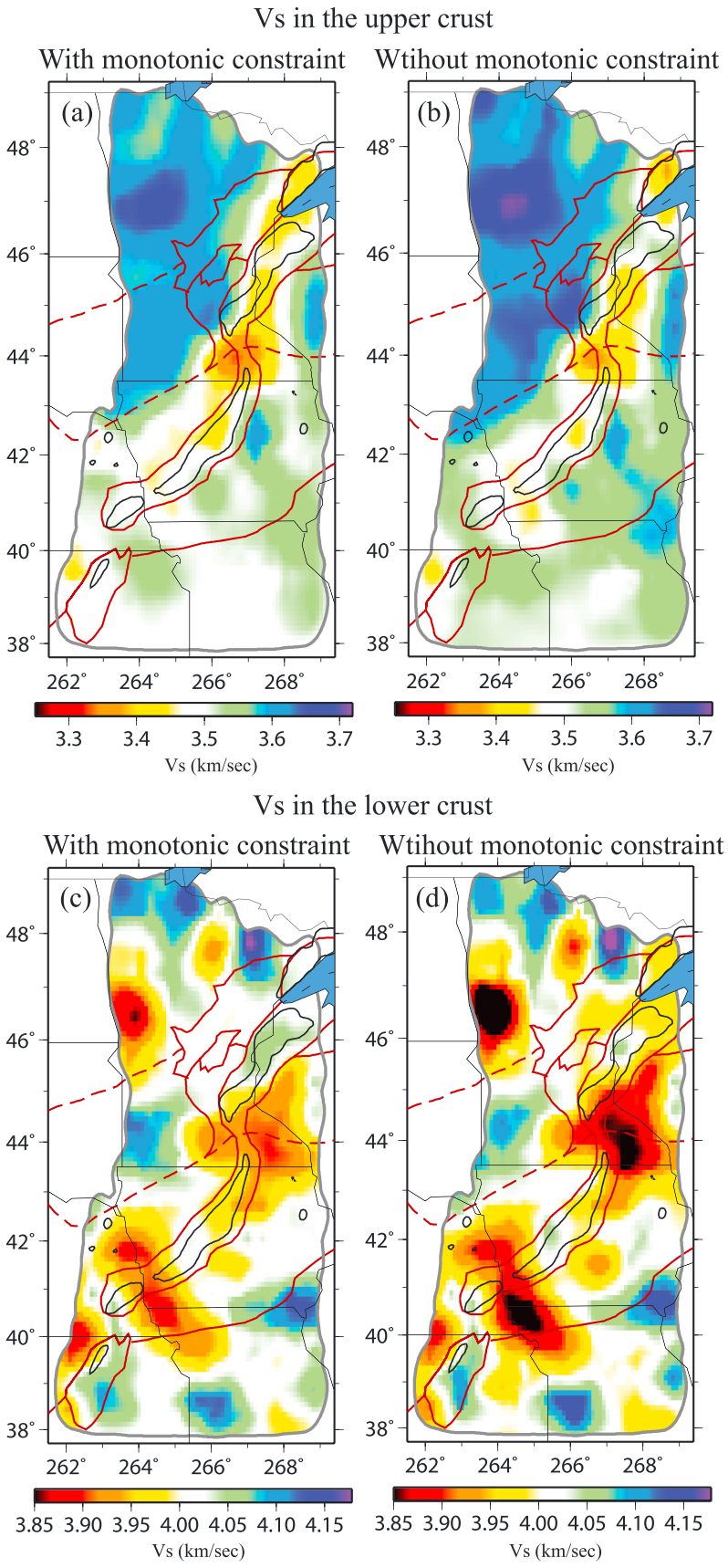

Figure 11. Comparison of upper and lower crustal velocities from inversions in which the monotonic constraint either has or has not been imposed. Velocities are averaged across the upper and lower 20% of crustal thickness in each case, respectively.

we speculate may be the case on the southern edge of the southern MCR. Nevertheless, the most likely cause of much of the variability in velocity structure in the uppermost mantle is compositional heterogeneity.

[51] An alternative interpretation of the relatively low Vs is a lower depletion in magnesium in the mantle. *Jordan* [1979] argued that magnesium depletion will lower density but increase seismic velocities in the upper mantle. Thus, the lower wave speeds observed between the Great Lakes and Spirit Lakes Tectonic Zones may be due to less depleted material from the mantle rejuvenation that occurred during the rifting. Beneath the MCR near Lake Superior, basalts have been observed that were generated from a relatively juvenile mantle source [*Paces and Bell*, 1989; *Nicholson et al*., 1997], indicating the possible emplacement of less depleted material at shallower depth from the upwelling during the rifting. This possible rejuvenation process may leave an enriched mantle remnant at depths greater than 100 km beneath the MCR and its surroundings (e.g., the craton margin domain), causing slower Vs compared to the rest of more depleted subcratonic lithosphere. *Schutt and Lesher* [2006], however, argued that mantle depletion would cause relatively little change in Vs in the upper mantle. Thus, the cause of the observed velocity variability in the uppermost mantle remains largely an open question that deserves further concerted investigation.

4.7. Effect of Smoothness and Monotonicity Constraints on Crustal Structure

[52] The results presented to this point and the interpretation that followed from them are based on the application of both velocity smoothness and monotonicity constraints in the crystalline crust. The earth may not be smooth or vary monotonically with depth so we consider here if there is evidence for either midcrustal discontinuities or vertical velocity minima in the crust in the study region.

[53] Evidence for midcrustal discontinuities would come from the inability to fit the receiver functions with a continuous, smooth model between the base of the sediments and Moho. We find that we have significant trouble fitting the receiver function at only four of the 122 stations used in this study: TA stations H37A, N36A, L37A, and K39A (identified in Figure 1). In all four cases, we believe the receiver functions are good and reflect reliable information beneath each point. Figure 10 presents the two worst fit receiver functions at TA stations H37A and N36A. In both cases, a Moho Ps converted phase near 6 s (Figures 10b and 10e) is well fit by the continuous, monotonic crustal model, but there are oscillations in the receiver function at earlier times at both stations that are not fit (red lines in Figures 10b and 10e) with this parameterization (red lines in Figures 10a and 10d). The introduction of a midcrustal discontinuity (blue lines in Figures 10a and 10d) does allow the receiver functions to be fit acceptably (blue lines in Figures 10b and 10e). Three conclusions are worth drawing from these observations. First, because there are only four isolated stations at which receiver functions are not well fit by the continuous, monotonic crustal model, there is no evidence that midcrustal discontinuities are general features of any of the tectonic zones in the region. Second, the models that result from the simplified parameterization agree with the models parameterized with a midcrustal discontinuity in crustal thickness, shallow crustal structure, and mantle structure. Therefore, the introduction of midcrustal discontinuities does not change the principal conclusions or arguments of this paper. Finally, discontinuous structures such as those shown by the blue line in Figure 10a are physically questionable. Further work is needed, presumably using data derived with a tighter station spacing (e.g., SPREE, *Stein* [2011]), which allows different receiver function stacking methods to be applied, to produce more realistic velocity profiles that fit the receiver functions at stations like H37A.

[54] We have also tested the effect of the monotonicity constraint by reperforming the inversion across the region without the constraint applied. Figure 11 presents a comparison between the models in the uppermost and lowermost crust with and without the imposition of the monotonicity constraint. In general, the results are very similar, although there is a tendency for the unconstrained model to have larger amplitudes particularly in the lower crust. The reason the monotonicity constraint has a relatively weak effect is because of our use of B-splines as basis functions in the crust. These splines automatically disallow local model excursions, and the monotonicity constraint merely makes this explicit. With the introduction of more freedom to the parameterization, perhaps through layerization or adding more B-splines, both local velocity minima and maxima would appear, but they are not required to fit the data.

5. Conclusions

[55] Based on 2 years of seismic data recorded by the USArray/Transportable Array stations that cover the western arm of the Midcontinent Rift (MCR) and its neighboring area, we applied ambient noise tomography using the eikonal tomography method and teleseismic earthquake tomography using the Helmholtz tomography method to construct Rayleigh wave phase velocity maps from 8 to 80 s across the region. By performing a joint Bayesian Monte Carlo inversion of the phase velocity measurements with receiver functions, we construct posterior distributions of shear wave speeds in the crust and uppermost mantle from which we infer a 3-D model of the region with attendant uncertainties to a depth of about 150 km. This model reveals three major features of the crust and uppermost mantle in this area.

[56] First, the observed free-air gravity field correlates with sediments and upper crustal structures in three ways. (1) A thick sedimentary layer contributes to the negative gravity anomalies that flank the MCR. (2) The slow upper crust at the gap between the northern and southern MCR masks the high gravity anomaly that runs along the rift. (3) Shear velocities in the uppermost crystalline crust are associated with a long-wavelength gravity anomaly that is observed across the study area. However, our 3-D model does not explain the existence of the gravity high along the rift because the crust beneath the MCR is seismically slow or neutral, on average. High-density anomalies must either be smaller than resolvable with our data or obscured by sediments. We believe the latter is the primary reason as the uppermost crust beneath the MCR probably contains both fast igneous rocks and slow clastic rocks, such that shallow igneous rocks dominate the gravity field while the clastic rocks dominate the shear wave speeds.

[57] Second, crustal thickening is found along the entire MCR, although along-axis variations exist and the gradient

Moho in the northern MCR makes uncertainties large there. Analysis of local faults and seismic reflection studies in this area provide additional evidence for a compressional inversion of the rift and crustal thickening during the Grenville orogeny [*French et al*., 2009]. Thicker crust and a deeper Moho cause a decrease in midcrustal shear wave speeds and in Rayleigh wave phase velocities at intermediate periods (15–40 s). Although the uppermost mantle beneath the MCR is faster than the average of the study region, velocity anomalies associated with the MCR are dominantly crustal in origin.

[58] Third, the seismic structure of the crust, particularly the shallow crust, displays discrete jumps across the three major Precambrian sutures across the study region. This implies that although the Superior Greenstone Terrane in the north collided with the Minnesota River Valley more than 2 Ga ago, preexisting structural differences beneath these two subprovinces are preserved. Other sutures (e.g., Spirit Lakes Tectonic Zone, Yavapai/Mazatzal boundary) also represent seismic boundaries in the crust. The mantle beneath the entire region is faster than for cratonic areas that have undergone significant tectonothermal modification and lithospheric thinning (e.g., North China Craton), with the Superior Greenstone Terrane being the least affected by events of tectonism across the region.

[59] In summary, the 3-D model presented here combined with other lines of evidence establishes that the MCR is a compressional feature of the crust. Presumably, the closing of the rift produced compressive stresses that thickened the crust beneath the MCR, advecting material downward in the crust under pure shear. The position of the slow thickened crust directly under the MCR suggests that crustal weakening during extension and subsequent thickening under compression occurred as pure shear [*McKenzie*, 1978], rather than under simple shear conditions. Simple shear would have resulted in a lateral offset between surface versus deep crustal features [*Wernicke*, 1985]. Finally, since the MCR has been inactive for long enough that thermal signals associated with tectonic activity should have long decayed, our results provide a useful context for distinguishing between compositional and thermal influences on seismic velocities in active continent rifts [*Ziegler and Cloetingh*, 2004].

[60] In closing, we note several topics for further research. (1) There is evidence at some stations for a midcrustal discontinuity, which deserves further focused investigation. (2) The USArray TA data do not provide ideal interstation spacing for receiver function analyses of the rift, and spatial aliasing of structures is possible. Finer sampling at select areas along the rift may appreciably improve the model. (3) Our model does not reveal structures deeper than about 150 km, which makes the determination of variations in lithospheric thickness difficult. (4) The physical cause of the low shear wave speeds in the uppermost crystalline crust (10 km depth) near the gap between the northern and southern MCR is unknown to us. (5) We also find mysterious the cause of very thin crust in the western Superior Province. (6) The spatial distribution of sharp versus gradient Moho across the region is fairly random and requires further investigation into the cause of this variability. (7) In particular, the tectonic cause of the gradient Moho beneath the northern MCR compared to the sharp Moho beneath the southern is unclear to us. These issues call for further work with a denser seismic array, such as the SPREE array which has already been installed in this area [*Stein et al*., 2011], as well as the input of other types of geophysical data. Nevertheless, the 3-D model provides a synoptic view of the crust and uppermost mantle across the region that presents an improved basis for further seismic/geodynamic investigation of the MCR.

[61] **Acknowledgments.** The authors thank the anonymous Associate Editor, an anonymous reviewer, and Brandon Schmandt for insightful criticism that aided in improving this paper as well as Suzan van der Lee for helpful comments. The facilities of the IRIS Data Management System, and specifically the IRIS Data Management Center, were used to access the waveform and metadata required in this study. The IRIS DMS is funded through the National Science Foundation and specifically the GEO Directorate through the Instrumentation and Facilities Program of the National Science Foundation under Cooperative Agreement EAR-0552316. Aspects of this research were supported by NSF grants EAR-1053291 and EAR-1252085 at the University of Colorado Boulder.

References

Anderson, R. R. (1992), The Midcontinent rift in Iowa, Ph. D. thesis, 324 pp., University of Iowa, Iowa City, Iowa.

Bassin, C., G. Laske, and G. Masters (2000), The current limits of resolution for surface wave tomography in North America, *EOS Trans. AGU*, *81*, F897.

Bastow, I. D., G. W. Stuart, J. Kendall, and C. J. Ebinger (2005), Upper-mantle seismic structure in a region of incipient continental breakup: Northern Ethiopian rift, *Geophys. J. Int.*, *162*(2), 479–493.

Bensen, G. D., M. H. Ritzwoller, M. P. Barmin, A. L. Levshin, F. Lin, M. P. Moschetti, N. M. Shapiro, and Y. Yang (2007), Processing seismic ambient noise data to obtain reliable broad-band surface wave dispersion measurements, *Geophys. J. Int.*, *169*(3), 1239–1260, doi:10.1111/j.1365-246X.2007.03374.x.

Bianchi, I., J. Park, N. Piana Agostinetti, and V. Levin (2010), Mapping seismic anisotropy using harmonic decomposition of receiver functions: An application to Northern Apennines, Italy, *J. Geophys. Res.*, *115*, B12317, doi:10.1029/2009JB007061.

Bodin, T., M. Sambridge, H. Tkalčić, P. Arroucau, K. Gallagher, and N. Rawlinson (2012), Transdimensional inversion of receiver functions and surface wave dispersion, *J. Geophys. Res.*, *117*, B02301, doi:10.1029/2011JB008560.

Bornhorst, T. J., J. B. Paces, N. Grant, J. D. Obradavich, and N. K. Huber 1988), Age of native copper mineralization, Keweenaw Peninsula, Michigan, *Econ. Geol.*, *83*, 619–625.

Boyd, N. K., and S. B. Smithson (1994), Seismic profiling of Archean crust: Crustal structure in the Morton block, Minnesota River Valley subprovince, *Tectonophysics*, *232*(1–4), 211–224, doi:10.1016/0040-1951(94)90085-X.

Braile, L. W., B. Wang, C. R. Daudt, G. R. Keller, and J. P. l. Patel (1994), Modelling the 2-D seismic velocity structure across the Kenya rift, *Tectonophysics*, *236*, 217–249.

Brocher, T. M. (2005), Empirical relations between elastic wavespeeds and density in the Earth's crust, *Bull. Seism. Soc. Am.*, *95*, 2081–2092 doi:10.1785/0120050077.

Cannon, W. F. (1994), Closing of the Midcontinent Rift—A far-field effect of Grenvillian compression, *Geology*, *22*(2), 155–158.

Cannon, W. F., and W. J. Hinze (1992), Speculations on the origin of the North American Midcontinent rift, *Tectonophysics*, *213*(1–2), 49–55.

Cannon, W. F., et al. (1989), The North American Midcontinent Rift beneath Lake Superior from GLIMPCE seismic reflection profiling, *Tectonics*, *8*(2), 305–332, doi:10.1029/TC008i002p00305.

Chandler, V. W., P. L. McSwiggen, G. B. Morey, W. J. Hinze, and R. R. Anderson (1989), Interpretation of seismic reflection, gravity, and magnetic data across Middle Proterozoic Mid-Continent Rift System, Northwestern Wisconsin, Eastern Minnesota, and Central Iowa, *AAPG Bull.*, *73*(3), 261–275.

Christensen, N. I., and W. D. Mooney (1995), Seismic velocity structure and composition of the continental crust: A global view, *J. Geophys. Res.*, *100*(B6), 9761–9788.

Dziewonski, A., and D. Anderson (1981), Preliminary reference Earth model, *Phys. Earth Planet. Int.*, *25*(4), 297–356.

Fox, A. J., (1988), An integrated geophysical study of the southeastern extension of the Midcontinent Rift System, M.S. thesis, 112 pp., Purdue University, West Lafayette, Ind.

French, S. W., K. M. Fischer, E. M. Syracuse, and M. E. Wysession (2009), Crustal structure beneath the Florida-to-Edmonton broadband seismometer array, *Geophys. Res. Lett.*, *36*, L08309, doi:10.1029/2008GL036331.

Frese, R. R. B., W. J. Hinze, and L. W. Braile (1982), Regional North American gravity and magnetic anomaly correlations, *Geophys. J. Royal Astron. Soc.*, *69*(3), 745–761.

Furlong, K. P., and D. M. Fountain (1986), Continental crustal underplating: Thermal considerations and seismic-petrologic consequences, *J. Geophys. Res.* (1978–2012), *91*(B8), 8285–8294.

Girardin, N., and V. Farra (1998), Azimuthal anisotropy in the upper mantle from observations of P-to-S converted phases: Application to southeast Australia, *Geophys. J. Int.*, *133*, 615–629.

Hammer, P., R. M. Clowes, F. A. Cook, A. J. van der Velden, and K. Vasudevan (2010), The Lithoprobe trans-continental lithospheric cross sections: Imaging the internal structure of the North American continent, *Can. J. Earth Sci.*, *47*(5), 821–857, doi:10.1139/E10-036.

Henk, A., L. Franz, S. Teufel, and O. Oncken (1997), Magmatic underplating, extension, and crustal reequilibration: Insights from a cross-section through the Ivrea Zone and Strona-Ceneri Zone, northern Italy, *J. Geol.*, *105*(3), 367–378.

Hinze, W. J., D. J. Allen, A. J. Fox, D. Sunwood, T. Woelk, and A. G. Green (1992), Geophysical investigations and crustal structure of the North American Midcontinent Rift system, *Tectonophysics*, *213*(1–2), 17–32, doi:10.1016/0040-1951(92)90248-5.

Hinze, W. J., D. J. Allen, L. W. Braile, and J. Mariano (1997), The Midcontinent Rift System: A major Proterozoic continental rift, *Geol. Soc. Am. Spec. Pap.*, *312*, 7–35, doi:10.1130/0-8137-2312-4.7.

Hollings, P., M. Smyk, L. H. Heaman, and H. Halls (2010), The geochemistry, geochronology and paleomagnetism of dikes and sills associated with the Mesoproterozoic Midcontinent Rift near Thunder Bay, Ontario, Canada, *Precambrian Res.*, *183*(3), 553–571, doi:10.1016/j.precamres.2010.01.012.

Holm, D. K., R. Anderson, T. J. Boerboom, W. F. Cannon, V. Chandler, M. Jirsa, J. Miller, D. A. Schneider, K. J. Schulz, and W. R. Van Schmus (2007), Reinterpretation of Paleoproterozoic accretionary boundaries of the north-central United States based on a new aeromagnetic-geologic compilation, *Precambrian Res.*, *157*(1–4), 71–79, doi:10.1016/j.precamres.2007.02.023.

Jones, C. H., and R. A. Phinney (1998), Seismic structure of the lithosphere from teleseismic converted arrivals observed at small arrays in the southern Sierra Nevada and vicinity, California, *J. Geophys. Res.*, *103*(B5), 10,065–10,090, doi:10.1029/97JB03540.

Jordan, T. H. (1979), Mineralogies, densities and seismic velocities of garnet lherzolites and their geophysical implications, in *The Mantle Sample: Inclusion in Kimberlites and Other Volcanics*, edited by F. R. Boyd and H. O. A. Meyer, pp. 1–14, AGU, Washington, D. C., doi:10.1029/SP016p0001.

Kanamori, H., and D. Anderson (1977), Importance of physical dispersion in surface wave and free oscillation problems: Review, *Revs. Geophys. Space Phys.*, *15*(1), 105–112.

Karato, S. (1993), Importance of anelasticity in the interpretation of seismic tomography, *Geophys. Res. Lett.*, *20*(15), 1623–1626, doi:10.1029/93GL01767.

Lebedev, S., J. Adam, and T. Meier (2013), Mapping the Moho with seismic surface waves: A review, resolution analysis, and recommended inversion strategies, *Tectonophysics*, doi:10.1016/j.tecto.2012.12.030.

Liang, C., C. A. Langston (2008), Ambient seismic noise tomography and structure of eastern North America, *J. Geophys. Res.*, *113*, B03309, doi:10.1029/2007JB005350.

Ligorria, J. P., and C. J. Ammon (1999), Iterative deconvolution and receiver-function estimation, *Bull. Seismol. Soc. Am.*, *89*(5), 1395–1400.

Lin, F.-C., and M. H. Ritzwoller (2011), Helmholtz surface wave tomography for isotropic and azimuthally anisotropic structure, *Geophys. J. Int.*, *186*(3), 1104–1120, doi:10.1111/j.1365-246X.2011.05070.x.

Lin, F.-C., M. P. Moschetti, and M. H. Ritzwoller (2008), Surface wave tomography of the western United States from ambient seismic noise: Rayleigh and Love wave phase velocity maps, *Geophys. J. Int.*, *173*(1), 281–298, doi:10.1111/j.1365-246X.2008.03720.x.

Lin, F.-C., M. H. Ritzwoller, and R. Snieder (2009), Eikonal tomography: Surface wave tomography by phase front tracking across a regional broad-band seismic array, *Geophys. J. Int.*, *177*(3), 1091–1110, doi:10.1111/j.1365-246X.2009.04105.x.

Mariano, J., and W. J. Hinze (1994), Structural interpretation of the Midcontinent Rift in eastern Lake Superior from seismic reflection and potential-field studies, *Can. J. Earth Sci.*, *31*(4), 619–628, doi:10.1139/e94-055.

McKenzie, D. (1978), Some remarks on the development of sedimentary basins, *Earth Planet. Sci. Lett.*, *22*, 108–125.

Moidaki, M., S. S. Gao, K. H. Liu, and E. Atekwana (2013), Crustal thickness and Moho sharpness beneath the Midcontinent rift from receiver functions, *Res. Geophys.*, doi:10.4081/rg.2013.e1.

Mooney, W. D., and M. K. Kaban (2010), The North American upper mantle: Density, composition, and evolution, *J. Geophys. Res.*, *115*, B12424, doi:10.1029/2010JB000866.

Morey, G. B., and P. K. Sims, (1976), Boundary between two Precambrian W terranes in Minnesota and its geologic significance, *Geol. Soc. Am. Bull.*, *87*(1), 141–152.

Nicholson, S. W., K. J. Schulz, S. B. Shirey, and J. C. Green (1997), Rift-wide correlation of 1.1 Ga Midcontinent rift system basalts: Implications for multiple mantle sources during rift development, *Can. J. Earth Sci.*, *34*(4), 504–520, doi:10.1139/e17-041.

Nielsen, C. A., and H. Thybo (2009), No Moho uplift below the Baikal Rift Zone: Evidence from a seismic refraction profile across southern Lake Baikal, *J. Geophys. Res.*, *114*, B08306, doi:10.1029/2008JB005828.

Nyblade, A. A., and R. A. Brazier (2002), Precambrian lithospheric controls on the development on the development of the East African Rift system, *Geology*, *30*(8), 755–758.

Paces, J. B., and K. Bell (1989), Non-depleted sub-continental mantle beneath the Superior Province of the Canadian Shield: Nd-Sr isotopic and trace element evidence from Midcontinent Rift basalts, *Geochim. Cosmochim. Acta*, *53*(8), 2023–2035.

Pavlis, N. K., S. A. Holmes, S. Kenyon and J. K. Factor (2012), The development and evaluation of the Earth Gravitational Model 2008 (EGM2008), *J. Geophys. Res.*, *117*, B04406, doi:10.1029/2011JB008916.

Pollitz, F. F. (2008), Observations and interpretation of fundamental mode Rayleigh wavefields recorded by the Transportable Array (USArray), *Geophys. J. Int.*, *173*, 189–204.

Pollitz, F. F., and J. A. Snoke (2010), Rayleigh-wave phase-velocity maps and three dimensional shear velocity structure of the western US from local non-plane surface wave tomography, *Geophys. J. Int.*, *180*, 1153–1169.

Ritzwoller, M. H., N. M. Shapiro, A. L. Levshin, and G. M. Leahy (2001), The structure of the crust and upper mantle beneath Antarctica and the surrounding oceans, *J. Geophys. Res.*, *106*(B12), 30,645–30,670.

Ritzwoller, M. H., F. C. Lin, and W. Shen (2011), Ambient noise tomography with a large seismic array, *C. R. Geosci.*, 13, doi:10.1016/j.crte.2011.03.007.

Saltzer, R. L., and E. D. Humphreys (1997), Upper mantle *P* wave velocity structure of the eastern Snake River Plain and its relationship to geodynamic models of the region (1978–2012), *J. Geophys. Res. 102*(B6), 11,829–11,841.

Schmus, W. R. (1992), Tectonic setting of the Midcontinent Rift system, *Tectonophysics*, *213*(1–2), 1–15, doi:10.1016/0040-1951(92)90247-4.

Schutt, D. L., and C. E. Lesher (2006), Effects of melt depletion on the density and seismic velocity of garnet and spinel lherzolite, *J. Geophys. Res.* (1978–2012), *111*, B05401, doi:10.1029/2003JB002950.

Shapiro, N. M., and M. H. Ritzwoller (2002), Monte-Carlo inversion for a global shear velocity model of the crust and upper mantle, *Geophys. J. Int.*, *151*, 88–105.

Shapiro, N. M., M. Campillo, L. Stehly, and M. H. Ritzwoller (2005), High-resolution surface-wave tomography from ambient seismic noise, *Science (New York, N.Y.)*, *307*(5715), 1615–8, doi:10.1126/science.1108339.

Shen, W., M. H. Ritzwoller, and V. Schulte-Pelkum (2013a), A 3-D model of the crust and uppermost mantle beneath the central and western US by joint inversion of receiver functions and surface wave dispersion, *J. Geophys. Res. Solid Earth*, *118*, 1–15, doi:10.1029/2012JB009602.

Shen, W., M. H. Ritzwoller, V. Schulte-Pelkum, and F.-C. Lin (2013b), Joint inversion of surface wave dispersion and receiver functions: A Bayesian Monte-Carlo approach, *Geophys. J. Int.*, *192*, 807–836, doi:10.1093/gji/ggs050.

Sims, P. K., and Z. E. Petermar (1986), Early Proterozoic Central Plains orogen: A major buried structure in the north-central United States, *Geology*, *14*(6), 488–491.

Stein, S., et al. (2011), Learning from failure: The SPREE Mid-Continent Rift Experiment, *GSA Today*, *21*(9), 5–7, doi:10.1130/G120A.1.

Thybo, H., and C. A. Nielsen (2009), Magma-compensated crustal thinning in continental rift zones, *Nature*, *457*, 873–876, doi:10.1038/nature07688.

Van Schmus, W. R., et al. (1993), Transcontinental Proterozoic provinces, in *Precambrian: Conterminous*, Geology of North America v. C-2, edited by J. C. Reed Jr. et al., p. 171–334, Geological Society of America, U.S.: Boulder, Colorado.

Vervoort, J. D., K. Wirth, B. Kennedy, T. Sandland, and K. S. Hatpp (2007), The magmatic evolution of the Midcontinent rift: New geochronologic and geochemical evidence from felsic magmatism, *Precambrian Res.*, *157*(1–4), 235–268, doi:10.1016/j.precamres.2007.02.019.

Wernicke, B. P. (1985), Uniform-sense normal simple shear of the continental lithosphere, *Can. J. Earth Sci.*, *22*, 108–125.

West, M., W. Gao, and S. Grand (2004), A simple approach to the joint inversion of seismic body and surface waves applied to the southwest U. S., *Geophys. Res. Lett.*, *31*, L15615, doi:10.1029/2004GL020373.

White, W. (1968), The native-copper deposits of northern Michigan, in *Ore Deposits of the United States, 1933-1967,* vol. 1, pp. 303–325, American Institute of Mining Engineers, New York.

Whitmeyer, S. J., and K. E. Karlstrom (2007), Tectonic model for the Proterozoic growth of North America, *Geosphere*, *3*(4), 220–259, doi:10.1130/GES00055.1.

Wilson, D., R. Aster, M. West, J. Ni, S. Grand, W. Gao, W. S. Baldridge, S. Semken, and P. Patel (2005), Lithospheric structure of the Rio Grande rift, *Nature*, *433*, 851–854.

Woelk, T. S., and W. J. Hinze (1991), Model of the midcontinent rift system in northeastern Kansas, *Geology*, *19*(3), 277–280, doi:10.1130/0091-7613.

Woollard, G. P. (1959), Crustal structure from gravity and seismic measurements, *J. Geophys. Res.*, *64*(10), 1521–1544.

Woollard, G. P., and H. R. Joesting (1964), Bouguer gravity anomaly map of the United States, map, 1:2,500,000, U.S. Geol. Surv., Washington, D.C.

Wright, H. E. (1962), Role of the Wadena Lobe in the Wisconsin Glaciation of Minnesota, *Geol. Soc. Am. Bull.*, *73*(1), 73–100, doi:10.1130/0016-7606.

Xie, J., M. H. Ritzwoller, W. Shen, Y. Yang, Y. Zheng, and L. Zhou (2013), Crustal radial anisotropy across eastern Tibet and the western Yangtze craton, *J. Geophys. Res. Solid Earth*, *118*, doi:10.1002/jgrb.50296.

Yang, Y., and M. H. Ritzwoller (2008), The characteristics of ambient seismic noise as a source for surface wave tomography, *Geochem. Geophys. Geosysyt.*, *9*, Q02008, doi:10.1029/2007GC001814.

Yang, Y., M. H. Ritzwoller, F.-C. Lin, M. P. Moschetti, and N. M. Shapiro (2008a), Structure of the crust and uppermost mantle beneath the western United States revealed by ambient noise and earthquake tomography, *J. Geophys. Res.*, *113*, B12310, doi:10.1029/2008JB005833.

Yang, Y., A. Li, and M. H. Ritzwoller (2008b), Crustal and uppermost mantle structure in southern Africa revealed from ambient noise and teleseismic tomography, *Geophys. J. Int.*, doi:10.1111/j.1365-246X.2008.03779.x.

Yang, Y., M. H. Ritzwoller, Y. Zheng, W. Shen, A. L. Levshin, and Z. Xie (2012), A synoptic view of the distribution and connectivity of the mid-crustal low velocity zone beneath Tibet, *J. Geophys. Res.*, *117*, B04303, doi:10.1029/2011JB008810.

Zartman, R. E., P. D. Kempton, J. B. Paces, H. Downes, I. S. Williams, G. Dobosi, and K. Futa (2013), Lower-crustal xenoliths from Jurassic kimberlite diatremes, upper Michigan (USA): Evidence for Proterozoic orogenesis and plume magmatism in the lower crust of the southern Superior Province, *J. Petrology*, *54*(3), 575–608, doi:10.1093/petrology/egs079.

Zheng, Y., W. Shen, L. Zhou, Y. Yang, Z. Xie, and M. H. Ritzwoller (2011), Crust and uppermost mantle beneath the North China Craton, northeastern China, and the Sea of Japan from ambient noise tomography, *J. Geophys. Res.*, *116*, B12312, doi:10.1029/2011JB008637.

Zhou, L., J. Xie, W. Shen, Y. Zheng, Y. Yang, H. Shi, and M. H. Ritzwoller (2012), The structure of the crust and uppermost mantle beneath South China from ambient noise and earthquake tomography, *Geophys. J. Int.*, doi:10.1111/j.1365-246X.2012.05423.x.

Ziegler, P., and S. Cloetingh (2004), Dynamic processes controlling evolution of rift basins, *Earth Sci. Rev.*, *64*, 1–50.